MACQUARIE UNIVERSITY

FACULTY OF SCIENCE AND ENGINEERING

The Effect of Camber and Yaw Angle on the Aerodynamic Performance of Rotating Wheels in Contact with the Ground

Kaustubh Sanjay Dongre

Master of Research

Submitted to the Department of Engineering of the Faculty of Science and Engineering, Macquarie University, Sydney Australia

April 2015

Supervisor: Dr Sammy Diasinos

Statement of Originality

I, Kaustubh Sanjay Dongre hereby declare that this submission is my own work and to the best of my knowledge it contains no materials previously published or written by another person, or substantial proportions of material which have been accepted for the award of any other degree or diploma at Macquarie University or any other educational institution, except where due acknowledgement is made in the thesis. Any contribution made to the research by others, with whom I have worked at Macquarie University or elsewhere, is explicitly acknowledged in the thesis. I also declare that the intellectual content of this thesis is the product of my own work, except to the extent that assistance from others in the project's design and conception or in style, presentation and linguistic expression is acknowledged.

Signed: 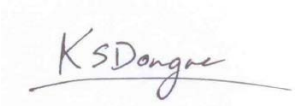

Date: 23/04/2015

Abstract

Within the automotive industry, there has been a strong push to develop more fuel efficient vehicles and the aerodynamic drag is a key parameter which significantly affects this. The airflow around wheels can contribute to up to 30% of aerodynamic drag, and therefore understanding the flow structures associated with them is expected to provide significant opportunities to make vehicles more fuel efficient. Previous studies in this field typically only considered a straight upright wheel despite most vehicles utilising some camber and steer. This study quantifies the effect of camber and yaw on the aerodynamic performance of rotating wheels while in contact with the ground. The results indicate that when camber is increased, the aerodynamic lift and drag both decreased, while introducing yaw angle increased both. For the range of camber angles considered, a maximum difference in lift and drag of 44% and 14% was observed compared to 17% and 33% respectively for yaw. The contact patch shapes for the cambered and yawed wheels were observed to be the key reason for the differences. It was concluded that the aerodynamic forces are more sensitive to camber in comparison to yaw and that the contact patch is the most critical geometric feature as the changes to the flow all stemmed from the variations observed at this location.

Acknowledgements

I would like to thank my supervisor Dr Sammy Diasinos for providing his guidance and assistance throughout the duration of this thesis. His wealth of experience and knowledge regarding CFD was of great help to me. Thank you for all the time you gave up for me and it was great to have a supervisor who had many of the same interests as I do. Additionally as a former Formula One aerodynamicist, exposing me to the tools and methods used in industry has given me a lot of confidence moving forward with my professional career.

I would also like to give many thanks to all my friends who have supported me throughout the duration of this project. I would especially like to thank Carmine and Wisam; you guys have been great mates and were really supportive throughout the project. Beers are on me now.

Finally, to Mum and Dad, thank you for all the support you gave me. I am truly grateful for everything you do to make my life the best it can be.

Table of Contents

List of Publications

Dongre K.S and Diasinos S. “Investigating the Wake Properties of a Rotating Wheel with Camber and Yaw using CFD”. 11th International Conference on Computational Fluid Dynamics in the Minerals and Process Industry, 7-9 December 2015, Melbourne Australia.

List of Figures

List of Tables

Nomenclature

Symbol/Abbreviation	Definition
C_L	Coefficient of Lift
C_D	Coefficient of Drag
C_P	Coefficient of Static Pressure
ρ	Density
P	Pressure
D	Wheel Diameter
ω	Specific Dissipation rate
k	Turbulent Kinetic Energy
x	Positive Flow Direction
Re	Reynolds Number
μ	Dynamic Viscosity
μ_t	Turbulent Viscosity
CFD	Computational Fluid Dynamics
CAD	Computer Aided Design
GCI	Grid Convergence Index
RANS	Reynolds-Averaged-Navier-Stokes

1 Introduction and Motivation

Within the automotive industry, there has been a strong push to develop more fuel efficient vehicles. The aerodynamic drag is a key parameter which can significantly affect the overall fuel efficiency of a vehicle. The airflow around the wheels can contribute to up to 30% of this aerodynamic drag, and therefore understanding the flow structures associated with a rotating wheel is expected to provide significant opportunity to make vehicles more fuel efficient. A more aerodynamic road vehicle will increase fuel efficiency and reduce overall running costs [1].

In an automobile, drag is affected by the frontal shape, the surface area, and most importantly by the wheels and flow disturbances underneath the car [2]. The rotating wheels and the various components which are exposed on the underside of an automobile create very large regions of turbulent flow. It is this increased turbulence which increases the drag. The effect of this is magnified as the vehicle's speed increases. In addition to this, the interaction of the flow from the wheels and underside with other components of the car can lead to other disturbances in the flow further affecting the overall drag. To get a better understanding of how to reduce the drag and improve aerodynamic performance, it is required that the various components that contribute to aerodynamic

performance are identified and analysed separately. For this investigation the focus is on the flow around isolated rotating wheels.

When considering the flow around wheels, one must first understand how the wheel is positioned and oriented relative to the free stream air. Angles which are used to define this are known as camber and yaw (toe and steering angle) [3]. These are shown in Figure 1.1 below.

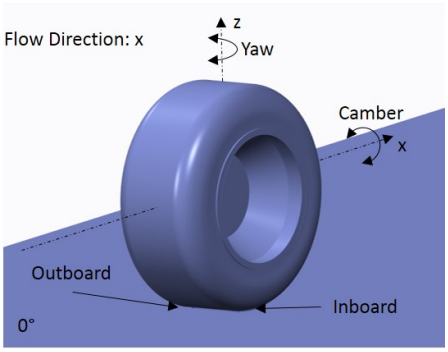

Figure 1.1: Camber and Yaw Angle Definition

Camber is a rotation about the x axis and yaw angle is defined as a rotation about the z axis. Smaller yaw angles are referred to as toe and are permanent. Yaw angles during steer are temporary and are usually larger. These angles are discussed further and in more detail in Section 3. These angles need to be investigated as they greatly affect the handling of a vehicle [3]. These angles are set in order to improve safety at higher speeds. Should these angles have a negative impact aerodynamically, these need to be understood so that they may be addressed. If a relationship between the aerodynamic forces and the angles was

to be established, the design of automobiles would be greatly improved. Manufacturers would be able to help optimise their vehicle aerodynamics for specific driving conditions.

This thesis presents a complete computational analysis investigating these parameters. Simulations were performed using commercial computational fluid dynamics (CFD) software ANSYS Fluent 15.0. Using the Fackrell [4] wheel geometry, simulations were performed whereby five different camber angles and seven different yaw angles were considered. Relationships between the aerodynamic forces and these angles were obtained and trends were observed and discussed. A comparison of the flow structures in the wake region of the wheel was constructed identifying areas in which the angles have a significant affect. Furthermore, the variation in contact patch shape due to camber and yaw was presented and discussed. The flow around the contact patch was compared and analysed.

2 Literature Review

This section provides background information regarding aerodynamics analysis techniques and how these are used for analysing wheel flows. In addition to this, past literature has been presented to showcase how far the field has progressed and what areas can be improved.

2.1 Aerodynamic Analysis Techniques

2.1.1 Computational Fluid Dynamics

Computational Fluid Dynamics is an analysis tool which has grown in popularity over the past few decades as it provided a method to perform flow experiments and aerodynamic analysis electronically. This increased the speed at which designs can be evaluated and reduced the costs associated with large scale experimental testing. CFD also provided a new way to help visualise the flow. Many flow features which were difficult to observe experimentally became visible because of this new tool.

CFD has been used effectively in aerospace, automotive, marine and mechanical fluid flow applications such as pumps. In order to construct a CFD model, first one must create a CAD model of the flow domain. This domain must then be

discretised. CFD utilises the fundamental Navier-Stokes flow equations to predict how the flow will move through the flow field.

In the automotive industry, CFD is widely used for both external and internal flow features including vehicle bodywork design, cooling systems and exhaust and engine optimisation. For automotive wheel flows, CFD made it possible to visualise the flow field in areas which were very difficult to observe experimentally, for example the within the spokes of a wheel rim. The simulations allowed the flow in the wake to be visualised and understood much more quickly. Several studies utilising CFD to gain an understanding of wheel flows have been performed and will be discussed in Section 2.2 below.

2.2 Automotive Wheel Aerodynamics

This section discusses the previous work pertaining to automotive wheel flows. Information regarding both experimental and computational studies of stationary and rotating wheels has been presented.

2.2.1 Isolated Wheel Studies

To gain a deeper understanding of the flow features and aerodynamic performance characteristics of automotive wheels, several studies ([4-27]) have been performed over the years which discuss and compare the airflow in front, on the surface and in the wake of both stationary and rotating wheels. Prior to 1975,

attempts were made to model rotating wheels in contact with the ground however due to the limitations of the experiments, reproducing the conditions of a rotating wheel was difficult. The key area of concern was the interface between the wheel and the ground. One such study was performed by Morelli [15] which utilised a stationary ground with a small recess in which a wheel was free to rotate. The setup was such that the tangential velocity of the wheel was always equal to that of the free stream. This wheel however was never in contact with the ground. Using a recessed area was Morelli's attempt to try and reproduce the tyre deformation effects due to the weight of a vehicle and contact with the road. This setup is shown in Figure 2.1 below.

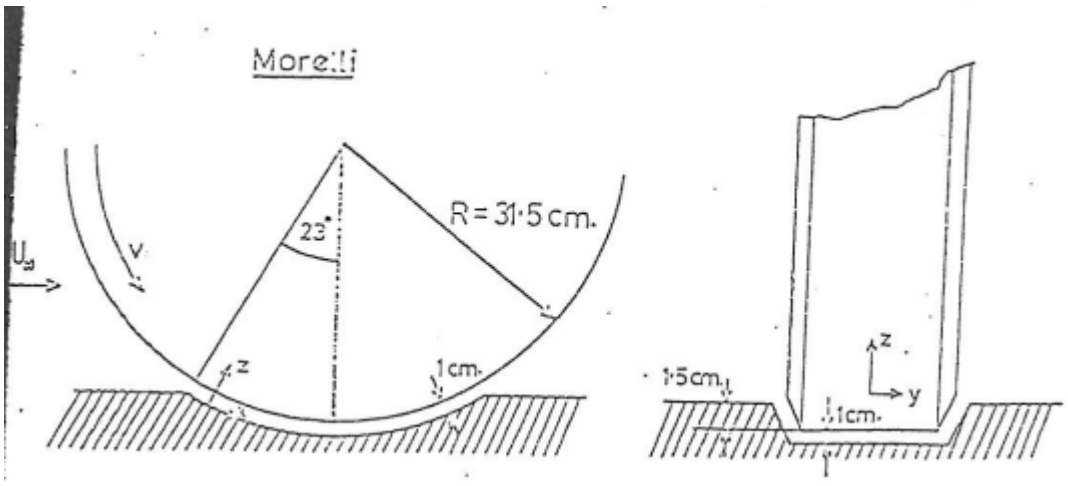

Figure 2.1: Experimental Configuration used by Morelli [15]

To measure the lift and drag on the wheel, Morelli [15] used a force balance for measurements and the frontal area of the wheel as his reference area. Using this method, the lift and drag coefficients were calculated to be -0.1 and 0.5

respectively for a Reynolds number of $1.3x10^6$ using a length scale of 0.04. It should be noted that from these results, Morelli [15] showed that his rotating wheel produced negative lift or downforce. To understand aerodynamic lift, very early experiments performed by NASA, then NACA, showed that a rotating cylinder, which was in essence a rotating wheel in free air, produced positive lift [28]. At the time, Moreli's result was significant as it suggested that that the interaction with the ground caused a drastic change to the flow, resulting in the forces changing direction. Morelli's result would later be shown to be incorrect.

In 1975, Fackrell [4] performed a number of experiments to investigate the flow around exposed grand prix style racing wheels. This study took a new direction in terms of modelling the wheel and road as well as calculating the forces on the wheel itself. Fackrell [4] was the first to use a complete moving ground with a freely rotating wheel. Unlike previous investigations, this meant that using a force balance was not possible. As a result of this a new method for calculating the lift and drag forces on the wheel was necessary. Fackrell [4] therefore decided to take static pressure measurements on the surface of the rotating wheel which were then converted to static pressure coefficients over various locations on the wheel. These coefficients were then integrated to determine the lift and drag over the wheel. This method eliminated the need for a force balance as the forces were determined mathematically after the experiments were performed [4].

Fackrell investigated a number of different wheel shapes which utilised different widths and shoulder profiles. He designated these widths as A, B and C and shoulder profiles as 1 and 2. All of the wheels he used had a diameter of 416mm. The wheels used by Fackrell contained no camber and experiments were performed at a Reynolds number of 5.3×10^3. The pressure distribution for the B2 wheel over the centreline is shown in Figure 2.2 below. This curve was used to calculate the lift and drag.

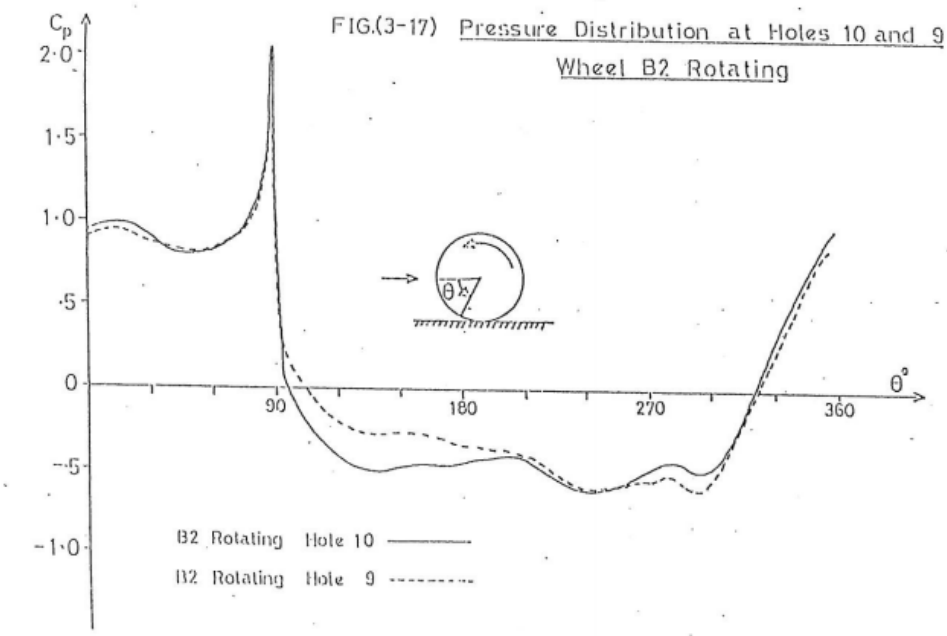

Figure 2.2: Pressure distribution over the rotating B2 wheel. Hole 10 is at centreline. [4]

For the rotating B2 wheel the calculated lift and drag coefficients were 0.65 and 0.85 respectively. These results showed and confirmed that an isolated rotating wheel in contact with the ground produced positive lift and not downforce as shown by Morelli [15]. Throughout his study Fackrell [4] also conducted

experiments for stationary wheels. Using the B2 wheel, it was observed that a stationary B2 wheel had lift and drag coefficients of 0.76 and 0.77 respectively. This showed that the stationary wheel produced approximately 17% more lift and 9% less drag. In addition to this, Fackrell showed that the width of the wheel did indeed have an effect on the overall lift and drag produced. Fackrell showed that the A2 wheel (narrower wheel) produced lift and drag coefficients of 0.64 and 0.90 respectively. Fackrell discussed concerns over the accuracy of the lift and drag results obtained for the B2 wheel however other flow features and observations remained consistent across the different wheel types. The trends observed when comparing stationary and rotating wheels were further confirmed using flow visualisation techniques such as smoke from which he was able to observe much higher flow separation over the top surface of the rotating wheel compared to the stationary one. It was also observed that due to the wheels rotation, the separation point on the top surface moved closer to the front of the wheel. Furthermore, two primary vortices were identified which stemmed from the bottom of the wheel. These can be seen in Figure 2.3 below.

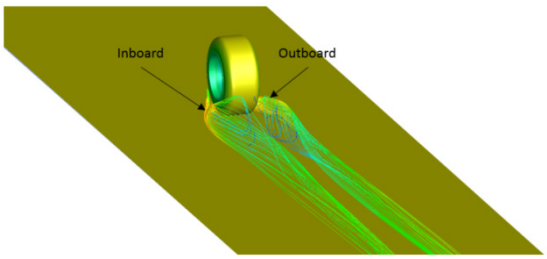

Figure 2.3: Velocity Streamlines showing the two primary vortices.

In addition to comparing the lift and drag of the various wheel configurations, Fackrell's result presented some interesting phenomena. From Figure 2.2 it can be seen that pressure coefficients higher than two were observed for the rotating wheel. Fackrell [4] explained that this phenomenon may have been due to the fact that the wheel and ground surfaces are moving closer together imparting energy into the flow. He then hypothesised that this convergence and increased pressure may cause a jetting flow upstream of the contact patch which may then move towards the sides of the wheel. This jetting flow would then form two primary, large counter rotating jetting vortices which strengthen and move downstream past the wheel. The existence of these jetting features however was not proven by Fackrell [4].

After the research by Fackrell was conducted, the importance of modelling the wheel and ground contact accurately became even more apparent. Therefore a study was performed by Cogotti [9] which investigated how the wheel's proximity to the ground affected the flow around it. This was an experimental investigation in which a wheel was placed in the free stream air and gradually lowered until the wheel was in contact with the ground. Throughout the investigation, static pressure measurements were recorded which provided a quantitative comparison. For the study, Cogotti [9] used a stationary approach with a piece of foam

between the wheel and the ground to try and model the interface at the contact patch.

From his experiments it was observed that when the wheel came closer to the ground, the flow started to accelerate through the gap displaying behaviour similar to a venturi nozzle. This resulted in a sharp pressure difference in his data, which showed that due to the slight gap the wheel produced negative lift or downforce. He also observed that the closer to the ground the wheel was, the more downforce was generated. Cogotti [9] also observed that the wheel would eventually reach a point where the flow would choke, thereby not allowing any flow to pass through the gap. At this point the wheel was observed to no longer produce downforce but to produce positive lift. This observation was very important and showed that modelling the contact of the wheel and ground accurately was key. Additionally it offered an explanation for the differing results obtained by Fackrell [4] and Morelli [15] previously. After the completion of this work, it was widely accepted that for modelling rotating wheels accurately, using a complete moving ground was the best method even though this was a difficult experimental apparatus to construct.

The existence of various vortical structures and their nature were confirmed by studies performed in 1988 by Bearman [29] *et al.* In this study, Bearman [29] further investigated the effects of a moving ground within a wind tunnel for

modelling the aerodynamics of road vehicles. He performed experiments utilising Fackrell's wheel and was able to identify and confirm the existence of the jetting features as postulated by Fackrell. Using a nine-hole pressure probe in the wake of the wheel, Bearman [29] documented the existence of the two large counter rotating vortices which travel downstream behind both the stationary and rotating wheel. He observed that the vortices deteriorate at a lower rate when the wheel is stationary. The two lower were shown to be the most dominant pair on the wheel [29].

To further investigate the flow in the wake region, Saddington [19] *et al.* presented an experimental analysis of the near wake of an isolated formula one wheel, using a technique known as three-component Laser Doppler Anemometry (LDA) [19]. This non-intrusive velocity measurement technique and was used to help characterise the flow and increase our understanding of the flow behind a rotating wheel. Experiments were performed using a closed circuit wind tunnel with a 2.74 m x 1.66 m test section equipped with a moving ground. His experiments were performed at a velocity of 30 m/s and a total of 613 data points were recorded.

From the data plane at 0.6D downstream of the wheel, four vortical regions were observed. Two upper vortices were identified from the upper wheel shoulders and two lower vortices were present. These lower vortices and their direction were

also confirmed previously by Bearman [29] *et al.* From Saddington's LDA results, it was observed that the two upper shoulder vortices of the wheel deteriorate much faster than those at the bottom of the wheel and are no longer visible on planes where x/D $\geq$ 1 downstream of the wheel. It was also noted that the upper vortex pair had merged with ground pair within one diameter downstream of the wheel. The lower vortices were shown to be much larger and more defined. The results presented align with what was observed by Fackrell further validating and enhancing his work.

In 2004, Mears [26] conducted a new study on an isolated rotating wheel in which he investigates the flow around a pneumatic go kart wheel. The reason for this was that Mears wanted to use a wheel that was more representative of what is used in reality. Using a go kart wheel allowed him to model a wheel which can deform based on the internal pressure and any external loads. Mears [26] used a similar method to Fackrell [4] in terms of recording static pressure measurements however he further improved on his methodology and utilised the modern resources he had to improve the quality of the measurements. Mears was able to use equipment which allowed him to better filter and analyse his experimental data. Mears also used a moving ground and performed experiments on both a stationary and rotating go kart wheel.

In Fackrell's experiments slip rings were used to get the surface static pressure measurements off the wheel [4]. This downside of this method was that it also produced a lot of electrical noise which manifested itself in the data. As a result, Mears has employed a setup which uses a wireless transmitter and receiver which will send the data to an external location away from the wheel. The on-wheel system operated by using an on-board battery, pressure sensors connected to pressure tappings, a microcontroller and a transmitter.

The system worked by first sampling the pressure sensor output voltage, which varies based on each pressure tapping, and converting this analogue output voltage to a digital signal. This is done on the wheel itself with a converter. The signal is then sent to a microcontroller which then transmits the data to a receiver located away from the wheel. On the receiver away from the wheel, the data is filtered and sorted and the digital data is then sent to a digital to analogue converter. The analogue voltage is connected to a "logging card" in a PC [26].

In addition to measuring the static pressure distribution over the wheel, Mears also used flow visualisation techniques such as smoke flow visualisation and also conducted experiments using particle image velocimetry (PIV) to try get a better understanding of the flow characteristics in the wake region of the wheel. For a straight, upright wheel, the stationary and rotating lift and drag coefficients

showed similar trends to what was observed by Fackrell [4]. The lift and drag coefficients for the stationary wheel were 0.60 and 0.73 respectively. And the lift and drag coefficients for the rotating wheel were 0.42 and 0.56 respectively. Furthermore Mears conducted an experiment to see what effect yawing the wheel would have on the flow. The wheel was yawed by an angle of 5 degrees. To achieve this condition the entire apparatus was yawed, including the moving ground, therefore the wheel itself was always rotating in line with the moving ground. After conducting his experiments the lift and drag coefficients were 0.35 and 0.59 respectively. Mears determined that a 5% reduction in lift and a 17% increase in drag were obtained, but Mears offered no explanation for the flow structure variations responsible for these changes and no indication was given for how the lift and drag would vary for other angles. As mentioned earlier, to achieve yaw, the entire apparatus was rotated, therefore it was not a true representation of a yawed wheel in contact with the ground but rather a crosswind experienced by the wheel. True yaw in this study represents the wheel being rotated about the z axis and the ground remaining in its original position with its original motion.

When comparing the static pressure distributions obtained by Mears and Fackrell, we see a key difference, in the form of a large negative peak as can be seen in Figure 2.5 below. This result may have been as a result of the filtering

and data sorting process used or could be as a result of different conditions at the contact patch compared to Fackrell.

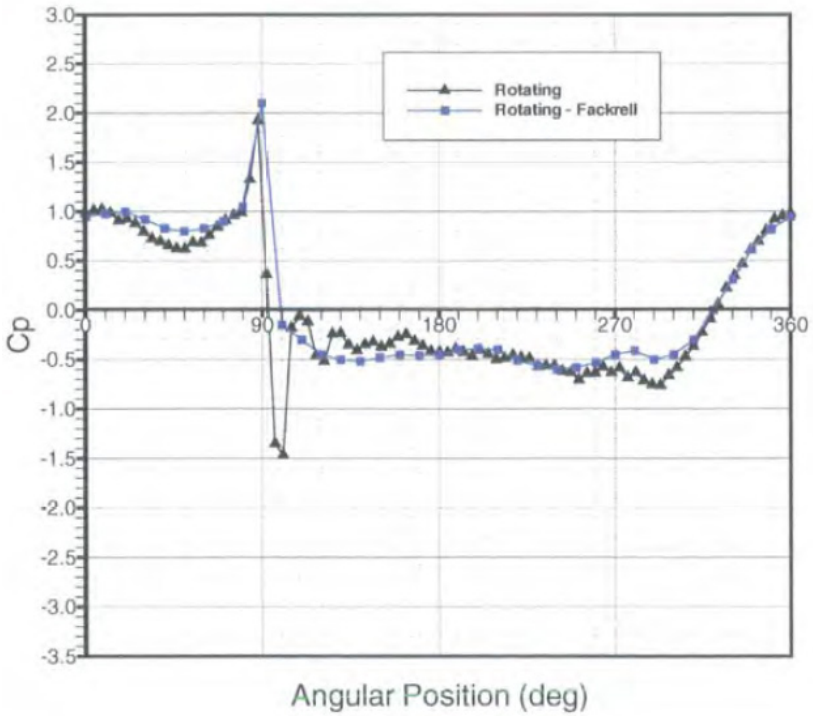

Figure 2.4: Static pressure distribution over the centreline of the rotating wheel. [26]

It was concluded that although Mears had access to new tools and methods, the variations due to the wheel deformations were not well discussed and hence the data obtained from Fackrell was still a more reproducible and comparable for this study

Over the last 25 years, investigations into wheel aerodynamics have started to utilise CFD as a tool to help identify flow features and to primarily improve our understanding of the flow wake region of wheels. In 1999, Axon [21] conducted a study which investigated the flow around a simplified wheel geometry which

shared the overall dimensions with the wheel used be Fackrell [4] however contained constant radius shoulders and no wheel rim. Axon used the commercially available CFD code, Fluent, to perform his simulations. Steady state RANS simulations were performed using both the standard k-ϵ and the RNG k-ϵ turbulence models. From the study it was found that the RNG k-ϵ model was more suitable when comparing the results to those obtained by Fackrell.

A key point to mention is that even in Axon's simulations, a C_P value greater than two was observed. This observation agreed with Fackrell [4], and Axon [21] further discussed Fackrell's hypothesis about the jetting flow and showed that the convergence of the wheel and moving ground indeed does help to form the primary jetting vortices.

In addition to his experimental work as detailed above, Mears [26] also conducted a series of simulations to investigate the flow around his exposed go kart wheel. The wheel used in the simulation was similar to Axon, in that it was a simplified wheel without a hub. The shoulder profile was measured using a "coordinate measuring machine" and was imported into the software. For the simulations, Mears created a tetrahedral mesh which consisted of 4.3 x 10^6 elements.

The mesh used by Mears is shown in Figure 2.6 below.

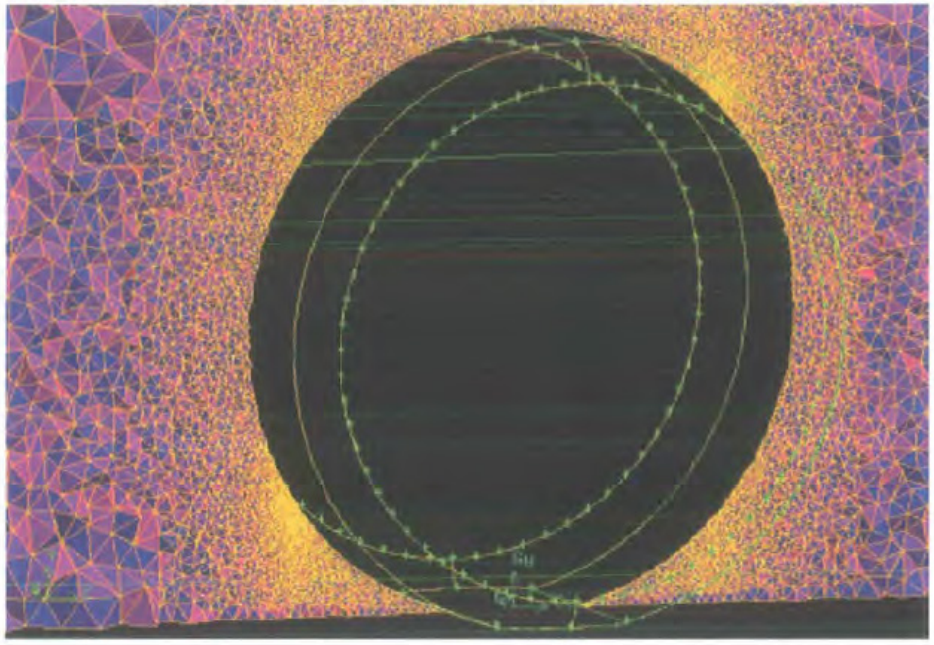

Figure 2.5: Tetrahedral volume mesh used by Mears [26]

Similarly to Axon, Mears used both the standard and RNG k-ϵ turbulence models. Mears however stated that the RNG turbulence model showed instabilities and did not converge very well. The standard model was shown to be more robust. Mears compared the static pressure coefficient obtained from his measurements over the centreline of the wheel to the CFD. The comparison is shown in Figure 2.7 below.

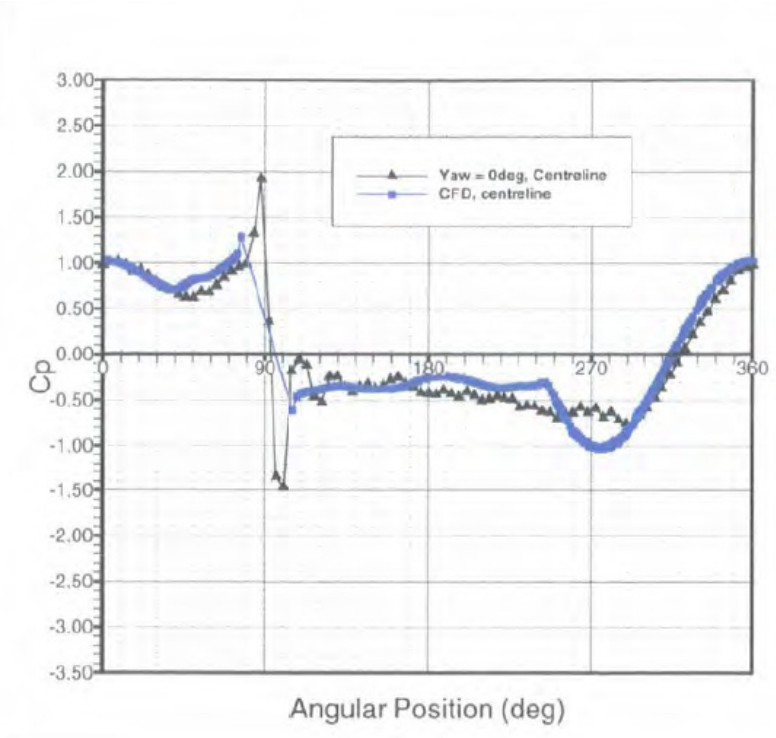

Figure 2.6: CFD and Experimental comparison. Static pressure coefficient over the centreline of the wheel [26]

From the comparison we can see that the CFD results did produce a positive pressure peak however with a lower magnitude than what was seen in the experiments. Furthermore the negative pressure peak has also been under predicted by the CFD. Based on the strategy used to model the contact patch of the wheel, the data near 90 degrees could not be obtained due to mesh restrictions and therefore the peak was omitted. The negative pressure peak at the separation point was also much larger than the measured experimental pressures.

Up until this point, the wheels used for computational investigations were all simplified versions of what was used by Fackrell. As a result only trends and similarities could be drawn. In 2006, McManus [14] and Zhang [14] conducted an investigation which used the exact geometry as used by Fackrell for the A2 wheel [14]. This geometry included the wheel hub and lips as well as an identical shoulder profile. This study was also the first to use an unsteady simulation approach. McManus [14] used a fully structured grid consisting of 2.94 million elements and two different turbulence models.

They used the Spalart-Almaras (S-A) and the Realizable k-ϵ (RKE) model. After this an Unsteady Reynolds Averaged Navier-Stokes (URANS) solution was initiated. This modelled the flow using the same parameters as a standard RANS for modelling the flow however added a transient approach to help resolve the flow structures. The Results were obtained for both a stationary and rotating wheel using a time step of 0.01 and the flow was allowed to develop for a further 10 time units. Flow features including the upper shoulder vortices, separation points and counter rotating jetting vortices were clearly visible. A schematic of the flow features observed by McManus [14] and Zhang [14] are shown in Figure 2.8 below.

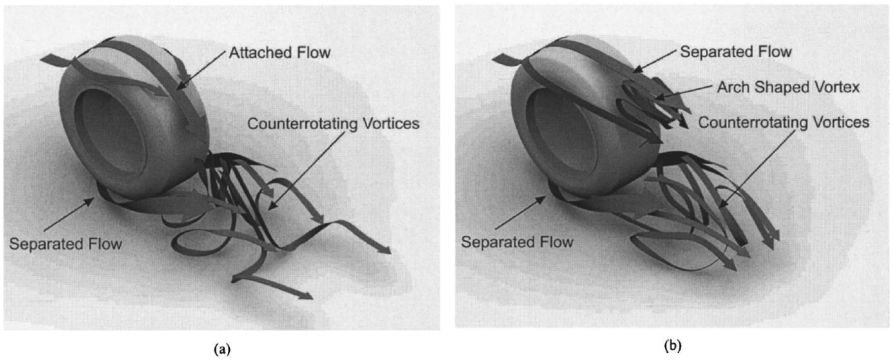

Figure 2.7: Comparison of the flow features of a stationary (a) and rotating (b) A2 Wheel. [14]

Furthermore, positive pressure peaks of 3.22 and 3.24 were observed when both the S-A and RKE turbulence models were used respectively. These values are considerably higher when compared to Fackrell's results. Also similarly to Mears [26] a substantial negative pressure peak was observed which suggests that a similar effect occurs in reverse just after the contact patch. This however was not observed in the experimental work performed by Fackrell [4]. The lift and drag predicted by McManus [14] and Zhang [14] were quite different. The lift and drag coefficients varied by approximately 44% and 15% respectively. The reasons for these variations were not discussed in detail and neither was the strategy used to model the contact patch of the wheel. It was highly likely that the modelling of the contact patch is greatly responsible for the variations as all of the primary flow structures stem from this location. However no detail into their modelling strategy for the contact patch was discussed therefore it is not possible to pin point any specific problems.

Further work utilising both CFD and experimental methods was conducted by Diasinos in 2009 [24]. He investigated the interaction of the flow between a rotating wheel and an inverted wing in ground effect. Initial simulations pertaining to isolated wheels were performed to identify the most ideal modelling strategy for a set of key parameters, in particular the contact patch of the wheel. Diasinos [24] conducted simulations in which the height of the contact patch was varied to determine the lift and drag sensitivity to this parameter.

For the simulations a fully structured grid was created using GAMBIT 2.3.16 and boundary conditions were set so as to match the experimental setup used by Fackrell [4]. The k-ϵ realizable turbulence model was used throughout his simulations. Steady state RANS simulations of Fackrell's wheel geometries were performed and the flow features including variations in flow separation and the vortical features were all observed. The flow structures observed aligned extremely well with what was presented by McManus [14] and Zhang [14]. From the simulations the lift and drag coefficient of the A2 wheel correlate very well and were within 1% of the coefficients calculated by Fackrell [4]. The flow structures around the A2 wheel as observed by Diasinos [24] are shown in Figure 2.9 below.

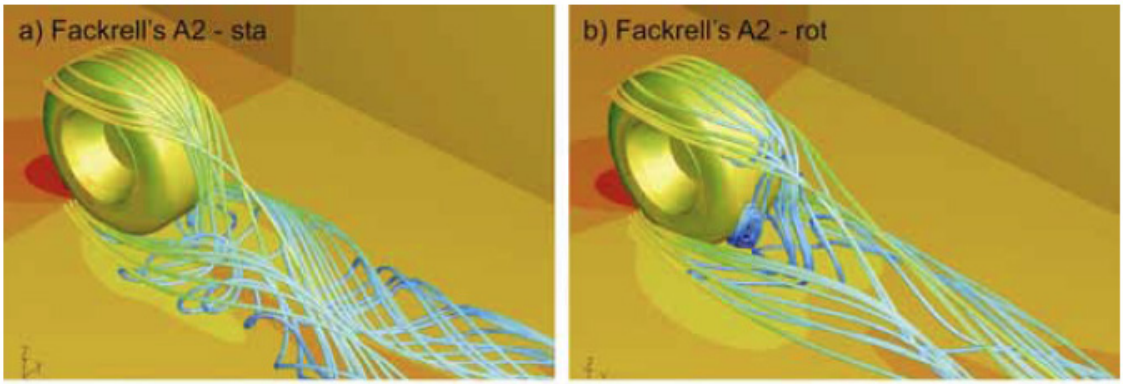

Figure 2.8: A2 wheel flow features as simulated by Diasinos a) Stationary b) Rotating [24]

Diasinos [24] also provided a new explanation as to why the two jetting vortices which were observed in the flow were sustained for a longer period of time and were more defined with wheel rotation. Diasnos [24] demonstrated that the primary wheel vortices are located depending on the distribution of flow entrainment from either the top or the side of the wheel wake. For the rotating wheel, the entrainment from the side of the wheel wake was shown to increase and from the top was shown to decrease. These variations in flow entrainment helped the primary vortices form higher and in a more central position. Additionally, he showed that the flow separation from the leading edge of the contact patch has a large effect on the formation of the jetting vortices. A relationship between the contact patch height and the strength of the jetting vortices was discussed showing that as the height of the contact patch was increased, the size and strength of the jetting vortices was reduced.

Furthermore, Diasinos discussed a relationship between the contact patch and its effect on the separation point over the wheel. It was discussed that the location of the separation point can be altered by the height of the contact patch and that the interaction of the flow behind the wheel as a result of the contact patch height is responsible for this change.

As it was shown that the flow separation at the leading edge of the contact patch had an effect on the jetting vortices it was easily observed that this affected the flow behind the wheel. Observations included that as the height of the contact patch was changed, the upper wheel wake was found to increase in height. This trend was also observed as the separation point on the wheel moved forward.

2.2.2 Camber and Yaw Angle

Since Diasinos' investigation several CFD studies have been undertaken which discuss the near wake region behind exposed rotating and stationary wheels ([1, 5, 7, 8, 10, 11, 22, 27]). As a result of the foundational work done by Fackrell and others, newer research has started to investigate how the flow features which have been established can change. Studies investigating wheel camber and yaw have been undertaken which demonstrate that the flow in the wake region will change significantly and ultimately affect the aerodynamic performance.

One such study was performed by John Axerio [7] *et al.* from Stanford University showcasing the flow in the near wake when using a stationary wheel which contained slight camber. Axerio [7] performed both steady state RANS simulations, LES simulations and performed experiments using particle image velocimetry (PIV) to help develop a better understanding of the near wake of a 60% scale stationary formula one wheel. The data presented by Axerio [7] showed consistent flow structures as predicted by Diasinos [24] and by Fackrell [4] for a stationary wheel, however the specific geometry used by Axerio has yielded some interesting results.

Camber angles of 2.5 and 3.25 degrees were tested and showed that the angle does indeed affect the flow in the wake region. It can be seen that the two lower vortices in these cases are no longer symmetric but slightly asymmetric. It was observed that the outboard vortex was slightly larger than the inboard vortex closest to the sting. This can be seen in Figure 2.10 below.

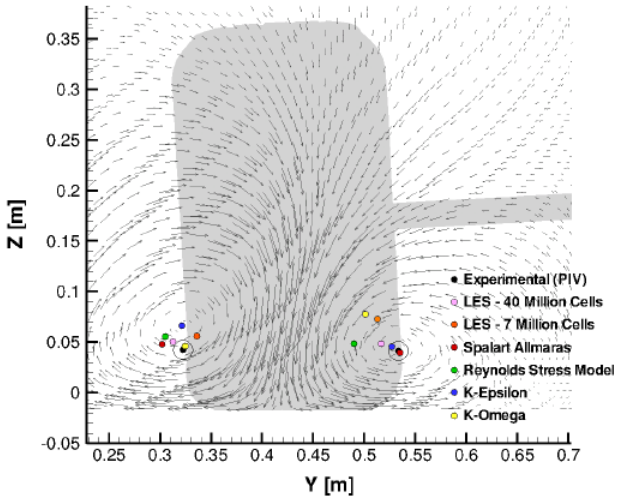

Figure 2.9: Comparison of Vortex core locations using LES, PIV and RANS data [7]

The work done by Axerio was done in conjunction with industry therefore no lift or drag data was presented. As such it was not known how much the camber angle affected the aerodynamic performance of the wheel.

Work similar to that performed by Axerio was done by Robin Knowles [13] *et al.* where a 40% scale champ car wheel was tested inside a wind tunnel equipped with a moving ground. The key difference between the two is that Knowles used a rotating wheel while Axerio did not. Knowles tested one straight wheel and one wheel with a camber angle of negative four degrees. In the near wake Knowles made some key observations comparing the straight wheel to the cambers wheel. As you move downstream from the cambered wheel, the outboard jetting vortex was seen to intensify and the vortices become more asymmetrical. Close to the wheel however, it was noticed that both upper vortices have a higher intensity

and were better defined and that the jetting vortices have a slightly lower vorticity compared to the straight wheel. Knowles also observed that the overall drag force decreases by approximately 12% due to the 4 degrees of camber [13]. No lift force data was presented.

This was the first study that has been observed to quantitatively compare the aerodynamic drag of a straight wheel to one with camber. However, only one angle has been tested, therefore any further trends could not be observed about the effect the angle has on the flow.

In addition to camber angle, the yaw angle of the wheel relative to the free stream flow is expected to create large differences in the wake profile of the wheel. In 2013, a CFD study was performed by Kothalawala et al. [30] where an isolated rotating wheel was placed in air far from a ground and yawed about the z-axis to see what effect this had on the flow around the wheel. For this investigation, the A2 geometry as described by Fackrell [4] was used. Both RANS and URANS simulations were performed and the realizable k-ϵ model was used. A free stream velocity of 70 m/s was used throughout the analysis which gave a Reynolds number of 1.9 x 10^6 with a length scale of 0.03.

After performing the simulations, the flow was observed to change significantly with yaw angle. It was observed that as the yaw angle increased the flow

structures behind the wheel became very asymmetrical which was expected with the flow over the upper wheel tread and shoulders being affected greatly. At high yaw angles the flow from inside the hub was seen to interact with the flow separating from the upper wheel shoulders creating further disturbances in the wake region. This can be seen in Figure 2.11 and in Figure 2.12 below.

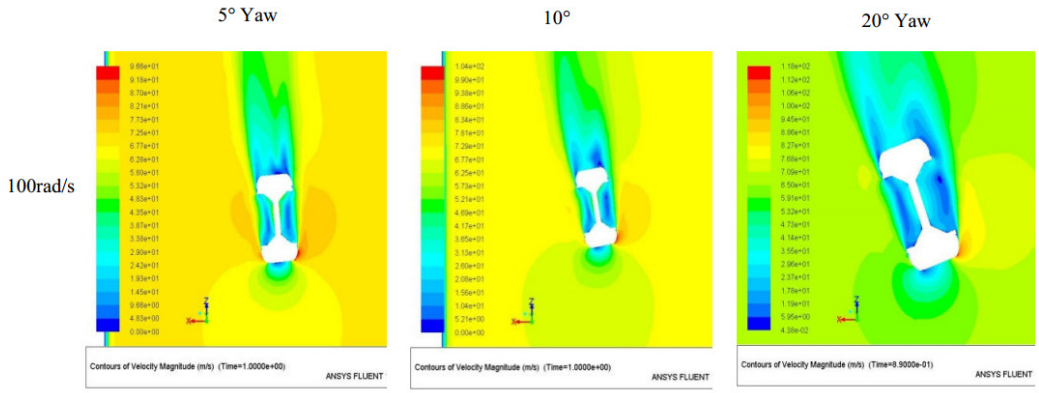

Figure 2.10: Velocity magnitude for the A2 wheel rotating at 100 rad/s as viewed from above for different yaw angles [30]

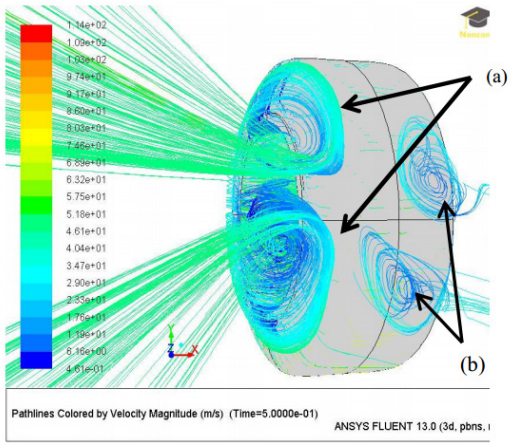

Figure 2.11: Interaction of the flow from the wheel hub and the wheel shoulders. a) Interaction of shoulder vortices with wheel hub flow b) Two additional vortices which form directly behind the wheel [30]

In addition to greatly disturbing the flow behind the wheel, the lift and drag also changes as a result. This is expected for drag as the frontal area is increasing as the wheel is yawed however as the wheel is not in contact with the ground, the wheel is shown to produce downforce which was also observed experimentally by Cogotti [9]. From the previous work published by Fackrell [4], Diasinos [24], Mears [26] and others, it is known that a rotating wheel in contact with the ground must produce positive lift. The data presented by Kothalawala is only valid for a case where the wheel is in the free stream and as such will not be considered valid for an automotive application. However this study provided a preliminary insight into the types of flow structures near the rim which may result due to yaw. The primary jetting vortices were not observed as expected.

2.3 Summary

Past research has provided key fundamental information regarding the flow around isolated wheels and how to model this experimentally and computationally. Investigations were performed to show the importance of a proper moving ground when conducting experiments for wheel aerodynamics. From this research, it was shown that there are a number of key areas around a wheel which have an effect on its aerodynamic performance. These areas primarily include the contact patch, the wheel shoulders and the top surface of the wheel. Furthermore the variations in the flow structures due to wheel rotation were

presented where the key differences are at the separation point on the top surface of the wheel and the jetting vortices.

The development of CFD and its use to gain an understanding about the flow around rotating wheels was also presented through a number of studies. These provided a more in depth look at the flow around the wheel and allowed for the visualisation of flow in areas which experimentally were not possible, most notably the separation around the leading edge of the contact patch.

In addition to these fundamental flow studies, current attempts to research the effect of camber and yaw angle was presented providing new information regarding how these parameters will affect the flow in the wake region and the lift and drag. It has been established that these parameters do have an effect on the flow, however previous work did not identify to what extend the effect is. Trends regarding the angles were not identified and further analysis was still required to be performed.

3 Project Aims and Description

The aim of this project was to quantify the effect camber and yaw angle has on the aerodynamic performance of rotating wheels which are in contact with the ground.

Camber and toe angles are set in order to aid the handling of all road vehicles while steering is a necessity for control. Camber and toe angles are specified for vehicles to improve and aid straight line stability and to improve handling characteristics at speed. Should these safety parameters have a detrimental effect on the overall aerodynamic performance off the wheel and therefore the fuel efficiency of the vehicle then it must be understood.

For an isolated wheel, when camber, toe or steer are applied, the shape of the wheels contact patch will change. Work conducted by Diasinos [24] has demonstrated the sensitivity that an isolated wheel has to the contact patch shape, the influence that this has on the primary vortices, the upper wheel tread separation point and consequently the lift and drag.

Camber angles are defined as the angle of tilt of the wheel when observed from directly in front of the wheel. These angles are symmetric about the centreline of the vehicle and can be defined as positive or negative angles. In this investigation only negative camber angles are considered. Throughout the thesis, the inner and

outer sides of the wheel are referred to as the inboard and outboard sides. Inboard refers to the side closest to the centre of the vehicle. A schematic of camber is shown in Figure 3.1 below.

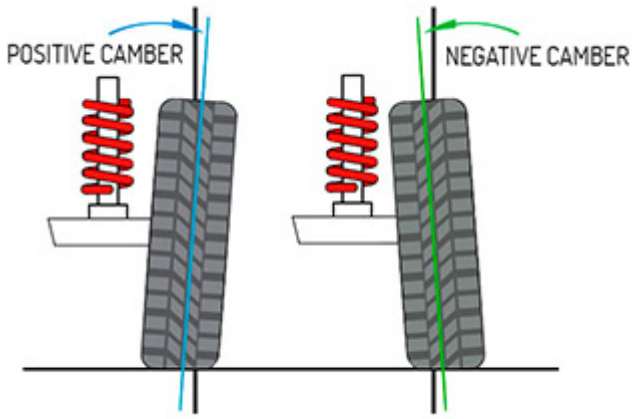

Figure 3.1: Diagram of Camber Angle [31]

Additionally, steering is expected to alter the frontal area exposed to the oncoming flow, a characteristic which is known to be a significant contribution to the drag generated by any body. As all road vehicles have some level of camber and toe, and that steering is a vital part of driving in everyday situations, it is important to investigate how the flow structures around rotating wheels change due to these parameters and how this might affect the overall aerodynamic performance of a vehicle and its fuel consumption. Toe angles are usually small yaw angles which are set to aid straight line handling.

In this investigation both small and large yaw or toe angles are considered to help identify a relationship between the angle and aerodynamic performance. A schematic of this angle is shown in Figure 3.2 below. All angles defined for this investigation are represented as toe-in angles for the right wheel as shown in the red box. Similarly as mentioned earlier, the inboard and outboard naming convention will also be used for yaw.

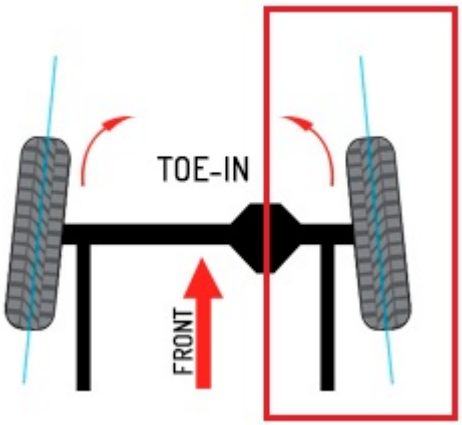

Figure 3.2: Yaw Angle Schematic [32]

For this project the wheel was cambered and yawed about an origin located at the centre of the wheel. This is shown in Figure 3.3 below.

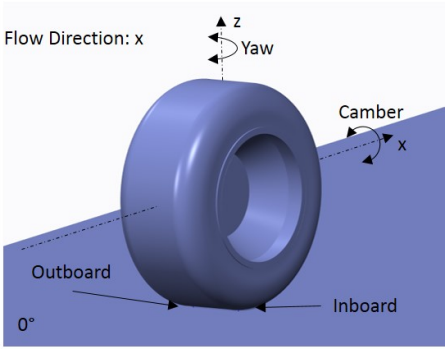

Figure 3.3: Camber and Yaw definition for this investigation

The key aims for this project are summarised in the following few points:

- Investigate and quantify the effect of camber angle on the aerodynamic performance of rotating wheels and determine the flow structure variations that are responsible for this.
- Investigate and quantify the effect of yaw angle on the aerodynamic performance of rotating wheels and determine the flow structure variations that are responsible for this.
- Identify which parameter (camber or yaw) has a greater impact on the overall aerodynamic performance of rotating wheels.

4 Computational Method and Modelling

4.1 Overall Procedure

The process of computational fluid dynamics can be summarised in a number of steps. These steps were followed throughout this research and are shown in Figure 4.1 below.

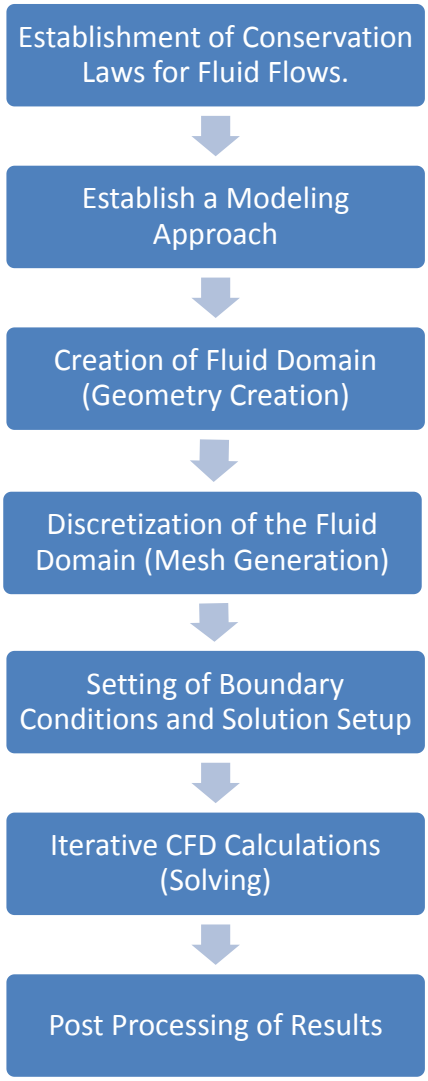

Figure 4.1: Procedure used for CFD investigation

4.2 Governing Equations

CFD is fundamentally governed by the laws of fluid mechanics. These are mathematical representations of fluid flow which were derived from the conservation laws of physics [33]. The laws which are used to characterise the movement and behaviour of fluid flows are as follows:

- Conservation of mass
- Conservation of momentum
- Conservation of energy, derived from the first law of thermodynamics.

The Navier-Stokes equations are used to mathematically represent this. These conservation criteria must be adhered to as the solution progresses. A detailed breakdown of the conservation laws are given in the subsequent sections.

For this investigation, compressible effects were not considered and as such the Conservation of Energy was not utilised.

4.2.1 Conservation of Mass

The conservation of mass or continuity condition expresses that the rate of change of mass within a fixed volume of fluid must remain the same as the rate of change of mass flux on the surface of the volume [33]. This is expressed as:

$$\frac{\partial \rho}{\partial t} + \nabla \cdot (\rho \mathbf{V}) = 0$$

Expressing the vector $\mathbf{V}$ using an x, y, z Cartesian coordinate system with corresponding velocities u, v and w, yields the following equation [33]:

$$\frac{\partial \rho}{\partial t} + \frac{\partial (\rho u)}{\partial x} + \frac{\partial (\rho v)}{\partial y} + \frac{\partial (\rho w)}{\partial z} = 0$$

In this investigation only incompressible flow is considered therefore the mass of the fluid does not change. As density remains constant and does not vary with time, the equation simplifies to:

$$\frac{\partial u}{\partial x} + \frac{\partial v}{\partial y} + \frac{\partial w}{\partial z} = 0$$

$$\therefore \nabla \cdot \boldsymbol{V} = 0$$

4.2.2 Conservation of Momentum

The conservation of momentum flow condition stems from Newton's second law. The sum of forces acting on a fluid volume is equal to the product of the mass of the volume and its acceleration. In the x direction this can be expressed as:

$$\Sigma F_x = m a_x$$

The mass of the control fluid volume is given as $\rho \Delta x \Delta y \Delta z$ and the acceleration of the control fluid volume can be expressed as the rate of change of its velocity u with respect to time. Therefore substituting these into the previous equation yields:

$$\Sigma F_x = \rho \Delta x \Delta y \Delta z \left(\frac{Du}{Dt}\right)$$

There are two main types of forces a fluid volume can experience. These are body forces and surface forces. Body forces include gravity, centrifugal forces and electromagnetic forces which may affect the entire body. For incompressible flows, the effects of body forces are regarded as negligible or irrelevant in comparison to the surface forces [33]. Surface forces on the other hand become apparent due to the stresses which are present on the faces of the volume. These stresses are known as normal and shear stresses.

For the velocity component u, which is in the x-direction, the surface forces are due to the normal stresses σ_{xx} and shear stresses τ_{yx} and τ_{zy}. The surface forces on a control volume are shown in Figure 4.2 below.

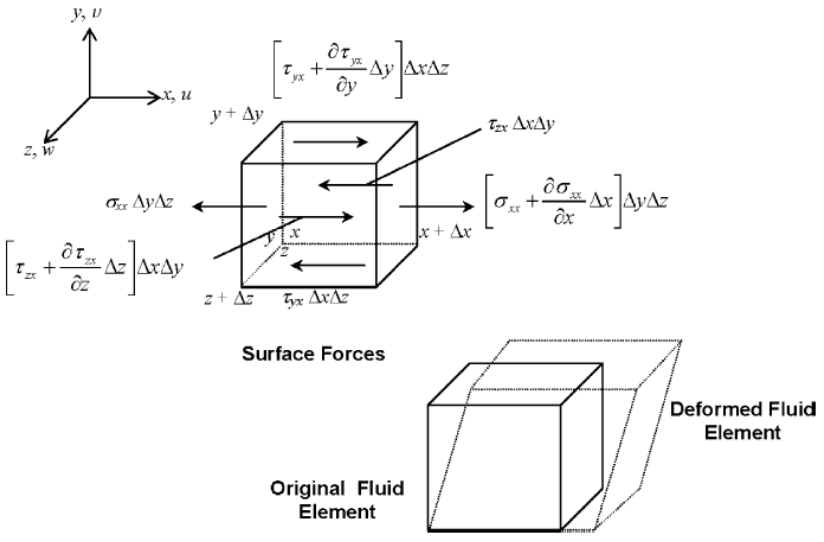

Figure 4.2: Surface Forces acting on the control fluid volume due to velocity component u and the resulting deformed volume. [33]

By combining the effects of these forces and the acceleration in the x direction, the momentum equation in the x direction becomes:

$$\rho \frac{Du}{Dt} = \frac{\partial \sigma_{xx}}{\partial x} + \frac{\partial \tau_{yx}}{\partial y} + \frac{\partial \tau_{zx}}{\partial z} + \sum F_x^{body\ forces}$$

Similarly, for the momentum in the y and z directions, the equation can be expressed as:

$$\rho \frac{Du}{Dt} = \frac{\partial \tau_{xy}}{\partial x} + \frac{\partial \sigma_{yy}}{\partial y} + \frac{\partial \tau_{zy}}{\partial z} + \sum F_y^{body\ forces}$$

and,

$$\rho \frac{Du}{Dt} = \frac{\partial \tau_{xz}}{\partial x} + \frac{\partial \tau_{yz}}{\partial y} + \frac{\partial \sigma_{zz}}{\partial z} + \sum F_z^{body\ forces}$$

If the fluid used is assumed to be Newtonian and isotropic fluid, the normal stresses σ_{xx} σ_{yy}, and σ_{zz} are now represented using the pressure (p) and normal viscous stress components (τ_{xx}, τ_{yy}, and τ_{zz}). Therefore for Newtonian and isotropic fluids, the normal stress components are expressed as the following:

$$\sigma_{xx} = -p + \tau_{xx} \qquad \sigma_{yy} = -p + \tau_{yy} \qquad \sigma_{zz} = -p + \tau_{zz}$$

When using a Newtonian fluid, both the linear and volumetric rates of deformation are proportional to the viscous stresses. To finally evaluate all of the stress components, firstly Newton's law of viscosity must be used to evaluate the viscous stresses with dynamic viscosity (μ) that relates linear stresses to linear

deformations and the second viscosity λ that relates stresses to the volumetric deformation respectively [33, 34].

The stress components are therefore expressed as the following:

$$\tau_{xx} = 2\mu\frac{\partial u}{\partial x} + \lambda\left[\frac{\partial u}{\partial x} + \frac{\partial v}{\partial y} + \frac{\partial w}{\partial z}\right] \qquad \tau_{xy} = \tau_{yx} = \mu\left(\frac{\partial v}{\partial x} + \frac{\partial u}{\partial y}\right)$$

$$\tau_{yy} = 2\mu\frac{\partial v}{\partial y} + \lambda\left[\frac{\partial u}{\partial x} + \frac{\partial v}{\partial y} + \frac{\partial w}{\partial z}\right] \qquad \tau_{xz} = \tau_{zx} = \mu\left(\frac{\partial w}{\partial x} + \frac{\partial u}{\partial z}\right)$$

$$\tau_{zz} = 2\mu\frac{\partial w}{\partial z} + \lambda\left[\frac{\partial u}{\partial x} + \frac{\partial v}{\partial y} + \frac{\partial w}{\partial z}\right] \qquad \tau_{yz} = \tau_{zy} = \mu\left(\frac{\partial w}{\partial y} + \frac{\partial v}{\partial z}\right)$$

Substituting these expressions for stresses into the three forms of the momentum equation and by defining the total body forces as a source term of momentum per unit volume per unit time (S_M), the equations for momentum in the x, y and z directions can now be expressed as the following:

$$\rho\frac{Du}{Dt} = -\frac{\partial p}{\partial x} + \frac{\partial}{\partial x}\left[2\mu\frac{\partial u}{\partial x} + \lambda\left(\frac{\partial u}{\partial x} + \frac{\partial v}{\partial y} + \frac{\partial w}{\partial z}\right)\right] + \frac{\partial}{\partial y}\left[\mu\left(\frac{\partial v}{\partial x} + \frac{\partial u}{\partial y}\right)\right] + \frac{\partial}{\partial z}\left[\mu\left(\frac{\partial w}{\partial x} + \frac{\partial u}{\partial z}\right)\right] + S_{M_x}$$

$$\rho\frac{Du}{Dt} = -\frac{\partial p}{\partial y} + \frac{\partial}{\partial y}\left[2\mu\frac{\partial v}{\partial y} + \lambda\left(\frac{\partial u}{\partial x} + \frac{\partial v}{\partial y} + \frac{\partial w}{\partial z}\right)\right] + \frac{\partial}{\partial x}\left[\mu\left(\frac{\partial v}{\partial x} + \frac{\partial u}{\partial y}\right)\right] + \frac{\partial}{\partial z}\left[\mu\left(\frac{\partial w}{\partial y} + \frac{\partial v}{\partial z}\right)\right] + S_{M_y}$$

$$\rho\frac{Du}{Dt} = -\frac{\partial p}{\partial z} + \frac{\partial}{\partial z}\left[2\mu\frac{\partial w}{\partial z} + \lambda\left(\frac{\partial u}{\partial x} + \frac{\partial v}{\partial y} + \frac{\partial w}{\partial z}\right)\right] + \frac{\partial}{\partial x}\left[\mu\left(\frac{\partial w}{\partial x} + \frac{\partial u}{\partial z}\right)\right] + \frac{\partial}{\partial y}\left[\mu\left(\frac{\partial w}{\partial y} + \frac{\partial v}{\partial z}\right)\right] + S_{M_x}$$

4.3 Numerical Procedure

A wide variety of computational fluid dynamics packages are commercially available for aerodynamic analysis. For this investigation the commercial software ANSYS Fluent 15.0 was used. This section outlines the procedure used to generate the computational models and provides information regarding how a good solution is generated.

4.3.1 Finite Volume Method and Discretization Schemes

In order to solve the various fundamental flow equations in CFD, an iterative finite difference method must be adopted. There are several types of finite difference schemes including, forward difference, backward difference and central difference methods [33]. ANSYS Fluent utilises the finite volume method which is a specific finite difference scheme used to calculate how flow moves throughout a domain. During pre-processing the flow domain must be split into a series of discrete volumes or cells. These volumes have a certain size and shape and can be generated by a number of different methods. By using this, the solver is able to calculate how the fluid travels through them. The quality of these cells is paramount to ensure the results are accurate [33, 34].

Ensuring high quality of cells becomes difficult when geometry becomes more complex. In order to capture complex geometries, more cells are usually required which can drastically increase the size of the model. In addition to this, it is important to capture regions of interest. Therefore, it is common for a grid to have refinement zones in various locations. When looking at aerodynamics, this is commonly done in the wake region behind a body. The most optimum grid is one which is of high quality, captures the geometry accurately, is refined in areas of interest and is small enough so as to be the most efficient in terms of computational resources required [33, 34].

Once the grid is defined, fluid properties and boundary conditions are also defined. This is very important step to ensure that the model represents the physical problem as closely as possible. During the solution, the governing flow equations are integrated over all of the volumes within the domain. These resulting integral equations are then converted to a series of algebraic equations through a process known as discretization. Once this is completed it ensures that the solver understands how to pass the information gathered from one control volume to the next. The problem can then be iteratively solved.

One of the most common methods of discretization is the upwind discretization scheme. When using the first order version this scheme, the quantities calculated at the cell faces are determined by assuming that the cell-center values of any

field variable represent a cell-average value and hold throughout the entire cell [35]. Values at the face of a cell are represented by the quantity ϕ_f and the values in the cell-center is denoted as ϕ. For most CFD applications, the second order upwind schemes are most commonly used. When second-order schemes are used, higher order accuracy is achieved at the faces of cells through the use of a Taylor series expansion of the cell-centred solution about the cell centroid [35]. When using second order upwind condition the values of ϕ_f are computed using the following equation:

$$\phi_f = \phi + \nabla\phi \cdot \vec{r}$$

Where ϕ and $\nabla\phi$ are the values at cell-centre and its gradient in the upstream cell respectively. The vector $\vec{r}$ represents the displacement vector from the upstream cell, from the cell centroid to the centroid of the face of the cell.

4.3.2 Turbulence Modelling

All flows in the real world can be characterised as either laminar or turbulent. The type of flow is defined by a parameter known as the Reynolds number (Re) which compares the ratio of inertial forces to viscous forces in the flow. For flows with low Reynolds numbers, the viscous forces are much higher than the inertial forces resulting in flow instabilities being easily dissipated and reduced, resulting in a smooth flow. These flows are known as laminar flows. As the Reynolds

number increases the inertial forces are amplified and at a point or critical Reynolds number, the smooth laminar flow becomes chaotic and unpredictable [34].

When focussing on the external aerodynamics of bluff bodies, almost all flows in this area are turbulent and chaotic in nature. These flows often contain areas of high flow separation and vorticity. For a rotating wheel in contact with the ground the wake is highly turbulent and very chaotic and CFD methods have had to be developed to help resolve these turbulent flow features. This section describes the most common turbulence models used for modelling external flows and discusses them in depth.

For RANS modelling, due to the chaotic nature of turbulent flow, the velocity parameter is replaced by an average velocity and velocity fluctuation term [34].

$$u = \bar{U} + U' \qquad v = \bar{V} + v' \qquad w = \overline{W} + w'$$

This ensures that the solving can progress within a bound helping to find a steady state solution. Similarly the pressure term is also replaced with an average and pressure fluctuation term.

$$p = \bar{P} + p'$$

4.3.2.1 k-Epsilon (k-ϵ)

The k-ϵ turbulence models are one of the most used and most validated models used in industry today. The k-ϵ model is a two equation model that uses the relationship between the turbulence quantity (k) and the rate of dissipation of turbulent kinetic energy (ϵ) [34]. Using these parameters the k-ϵ turbulence model has the ability to effectively resolve turbulent structures in the wake region behind objects. The standard k-ϵ model however, has some difficulty resolving highly vortical structures however most fluctuating flows can be easily visualised. Another area which the standard model does not perform the best is close to or on a boundary [34].

As a result of this, the newer k-ϵ Realizable model was developed. This model has several improvements in comparison to the existing standard turbulence model. Two important differences compared to the standard model are that a new formulation for turbulent viscosity was created and the transport equation for dissipation rate was changed. In the standard and RNG models the eddy viscosity (μ_k) is calculated as follows [34]:

$$\mu_k = \rho C_\mu \frac{k^2}{\epsilon}$$

The two transport variables are k and ϵ. Where the realizable model differs from the standard and RNG models is the C_μ term. In the standard and RNG models

this is a constant value where as in the realizable model, this is computed as a function of mean strain and rotation rate.

By changing this formulation, the realizable model has made marked improvements in a number of areas. A key area where it performs better is in regions of flow separation. The realizable model more accurately predicts separation, boundary layer flows and flows which involve large amounts of rotational components. In recent years this model has been used extensively for automotive aerodynamics such as the work done by McManus et al. [14] and Diasinos [1, 24]. In all investigations, they showed that the Realizable k-ϵ model matched the experimental work better than other models.

One area which must be taken into account is the fact that the k-ϵ model requires a near-wall correction since the model has always been designed to be more effective in the freestream. To ensure the boundary layer is modelled accurately the y^+ condition is used. This condition is shown below:

$$y^+ = \frac{\rho u_\tau y_p}{\mu}$$

Where,

ρ = the density of the fluid

μ = dynamic viscosity

u_τ = friction velocity

y_p = distance to the nearest wall

Using this condition, one can now determine the best near wall correction required. The closer the y^+value is to zero, the better the near wall performance when trying to model the viscous sublayer. Using the parameters stated above the formula was used to calculate the height of the first cell required in the mesh to allow for a $y^+ \leq 1$.

4.3.2.2 k-Omega (k-ω)

The standard k-ω model using in ANSYS Fluent is an empirical model based on the model transport equations for turbulent kinetic energy (k) and the specific dissipation rate (ω) [35]. This can be thought of as the ratio of ϵ to k. This model has been modified a number of times with the most important being the modification of the production terms of both k and ω [35]. This has improved the accuracy of the model for predicting free shear flows. The standard model however was designed to operate within low Reynolds numbers therefore its strength is observed when observing flow features near a boundary in the viscous layers. At higher Reynolds numbers however, the model underperforms in both force prediction and resolving highly turbulent flow structures.

To counteract this, the shear-stress transport (SST) version of the model was created. The SST model was first developed by Menter in 1994 [36] to blend the characteristics of the standard k-ω model and the standard k-ϵ model together.

This was to provide accurate simulation at the through the boundary layer on a wall and a better solution in regions of turbulence in the freestream.

The major ways in which the SST model differs from the standard model is that there is a gradual change from the standard k-ω model in the inner regions of the boundary layer to the higher Reynolds number of the k-ϵ model at the outer edge of the boundary layer and in the free stream. In addition to this there was a modification made to the turbulent viscosity formulation [35].

The modified turbulent viscosity (μ_t) is given below [35].

$$\mu_t = \frac{\rho k}{\omega} \frac{1}{\max\left[\frac{1}{\alpha*}, \frac{SF_2}{\alpha_1 \omega}\right]}$$

Where $\alpha*$ is a dmaping coefficient for the turbulent viscosity which utilises a low Reynolds number correction, S is the magnitude of strain rate, F_2 is a blending function which is formulation using both k and ω and takes into account the location of surfaces and their proximity to one another. The value α_1 is a constant which is set to be 0.31.

This model was tested by Menter [36] to predict the separation point over a wing and to look at the wake behind a cube. This model is being used more extensively in the aviation industry for aerofoil analysis however it still has areas which need to be improved for regions with high turbulence [33, 34].

4.3.2.3 Spalart-Allmaras

The Spalart-Allmaras (S-A) model is a one equation model developed in 1992 which solves a modelled transport equation for the turbulent kinetic eddy viscosity [35, 37]. This model was specifically designed for aerospace applications involving wall bounded flows and was shown to provide good results for boundary layers subjected to adverse pressure gradients. This model is also used for turbomachinery applications. This model requires the boundary layer to be properly resolved similar to the realizable k-ϵ model and requires that y^+should be less than or equal to 1. The newer forms of the model used in ANSYS Fluent also allow for a y^+ independent simulation [35]. This model is advantageous due to the fact it is computationally very efficient. This model uses a local approach to calculating turbulent features, in other words the solution at other points in the domain does not affect any other solution points. Therefore this model can be widely used with a number of different mesh types and the results should remain consistent across all simulations.

The equation for the turbulent eddy viscosity is given as:

$$\mu_t = \rho \vec{v} f_{v1}$$

Where $\vec{v}$ is the transport variable and is identical to the turbulent kinematic viscosity. At any wall however, this value is set to zero [35]. $f_{v1}$is specified as the viscous damping function and is expressed as:

$$f_{v1} = \frac{\chi^3}{\chi^3 + C_{v1}^3}$$

Where, $C_{v1}$is a constant and has a value of 7.1 and χ is a ratio of the transport variable to the molecular kinematic viscosity. This ratio is given by:

$$\chi = \frac{\vec{v}}{v}$$

4.3.3 Solution Method

Within ANSYS Fluent both a pressure based and a density based solver is offered. The pressure based solver is the most widely used for incompressible flows, however for flows where compressible effects are significant, the density based solver is recommended. For this investigation, compressibility effects were not considered at all therefore the pressure based solver was used throughout. This solver ensures that the conservation of mass is maintained throughout the domain by solving a pressure equation [33, 34].

The pressure based solver can be utilised using both a separated and coupled approach to solving the velocity and pressure equations throughout the fluid. The Semi Linked Method for Pressure Linked Equations or SIMPLE algorithm is the simplest and most commonly used solution algorithm. This uses a relationship between velocity and pressure equations to ensure continuity is met and to produce the pressure field.

This solution is then looped and solved continuously for a number of iterations until a converged solution is obtained. This process is shown in Figure 4.3 below.

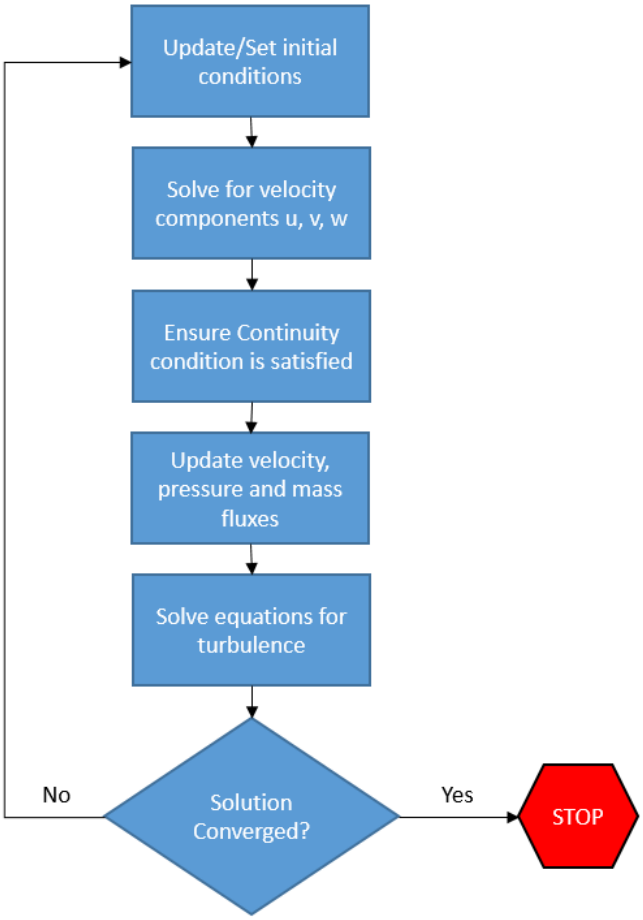

Figure 4.3: Solution procedure for the pressure based SIMPLE algorithm

Another form of the SIMPLE algorithm is known as SIMPLE-Consistent or SIMPLEC. This variant of the algorithm utilises a different face flux correction. This form of the algorithm has been found to show an improved rate of convergence in comparison to SIMPLE however the solving time per iteration also increases. As mentioned previously, a coupled approach to solving the pressure and velocity equations can also be utilised.

This method solves a coupled series of equations which comprise of the pressure based continuity equations and the conservation of momentum equations. By doing this, the pressure and velocity components are solved simultaneously, resulting in much faster convergence rates. The drawback of this algorithm is that it requires 1.5 to 2 times as much RAM as compared to the SIMPLEC algorithm. Additionally when using this algorithm, the solution tended to diverge far more easily. This may have been due to the complexity of the flow including features like vortex shedding which made it difficult to simultaneously solve the required equation. This was a surprise given that based on the literature it was said to be a great improvement over the SIMPLE and SIMPLEC algorithms. As a result of this, the SIMPLEC algorithm was used throughout the project for all simulations.

4.3.4 Solution Convergence

To ensure the solution obtained is of an acceptable standard, convergence criteria must be incorporated. Convergence of the solution can be defined in a number of ways for example using the steady state error and how the forces within the domain are changing over time. For this investigation, the steady state solution was said to have converged enough once oscillatory behaviour was observed within the force residuals and by monitoring the scaled residuals of velocity and continuity. The problem of wheel flows is highly transient, time constraints for this study limited modelling to RANS approaches only. All oscillations were

regular and all occurred within a range of 1%. When the force output showed oscillatory behaviour, this meant that the flow was repeating itself over a number of iterations. In reality this corresponded to generation and shedding of vortices coming off the wheel. In addition to oscillatory behaviour, the scaled residuals for velocity were monitored to ensure they were below 10^{-5} and that they were also no longer changing.

4.3.5 Model Description

4.3.5.1 Geometry Creation

The geometry was modelled using 3D computer aided design software Creo Parametric 2.0. The wheel models were generated using surfaces and the dimensions for the model were chosen such that they matched the experiments performed by Fackrell. The wheel chosen for this investigation was the A2 wheel.

The wheel had a diameter of 416 mm and a width of 191 mm. The rim profile is slightly asymmetric so as to accurately represent the wheel used in reality. The rim was simplified as a solid rim which was sized and located so as to represent a grand prix racing style wheel. The contact patch of the wheel was modelled using a similar approach to that used by Diasinos with a step height of 0.0028D [24].

The completed wheel geometry with dimensions and the contact patch are shown in Figure 4.4 and Figure 4.5 below.

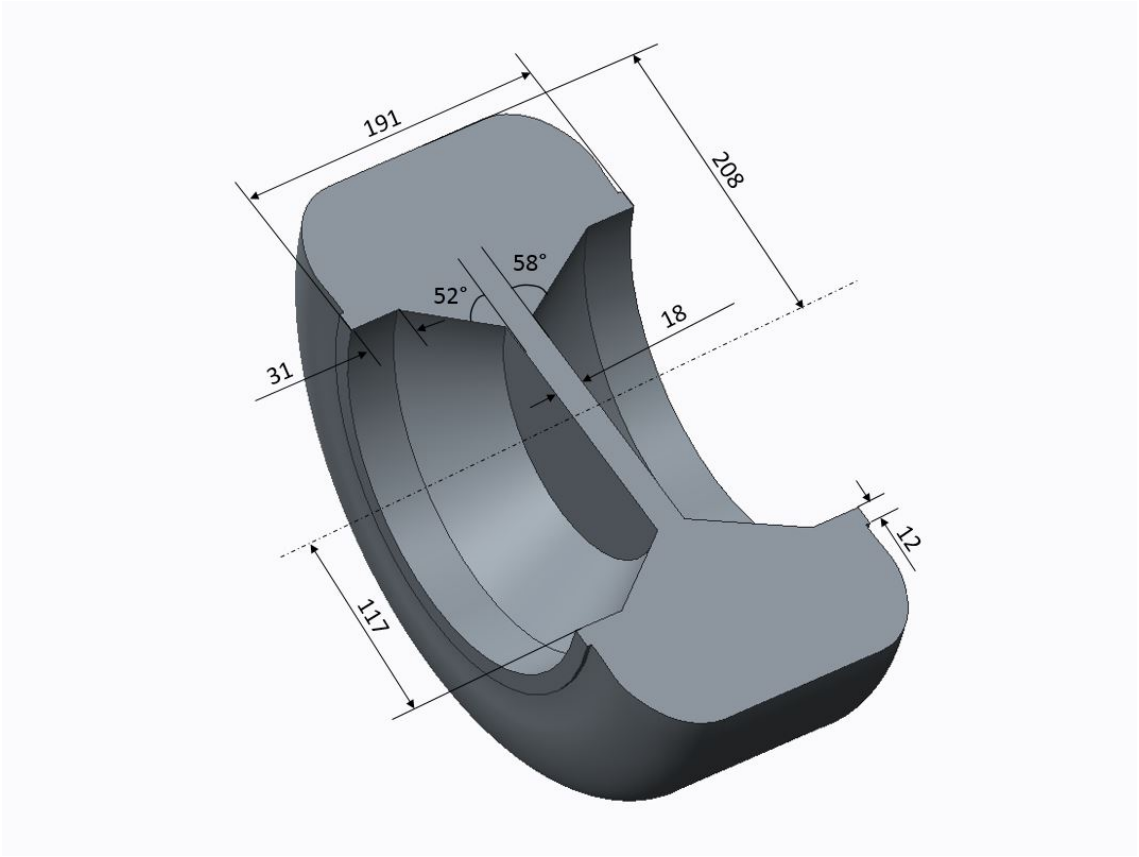

Figure 4.4: Fackrell A2 Wheel Geometry. All dimensions in mm

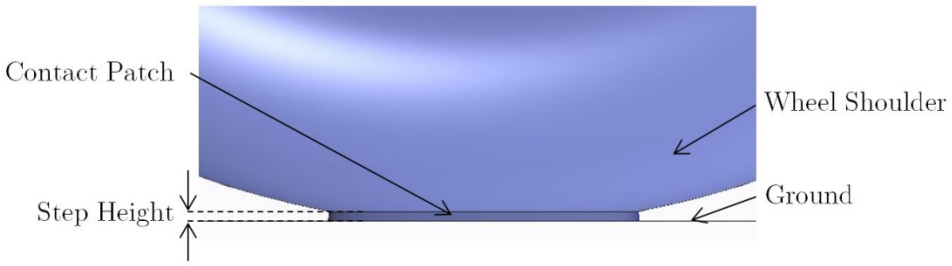

Figure 4.5: Contact Patch with step height 0.0028D

The size of the fluid domain was made so as to match Fackrell's wind tunnel cross-section with dimensions 1524 mm x 1219 mm (WxH) [4]. An inlet position of 10D in front of the wheel and an outlet position of 20D behind the wheel were chosen so as to ensure the inlet and outlet positions would not affect the solution

at the wheel. It was shown that extending the inlet an outlet positions did not affect the solution by more than 0.45%. The sizing of the domain was investigated in detail and is discussed in the following chapter. The final fluid domain is shown in Figure 4.6 below.

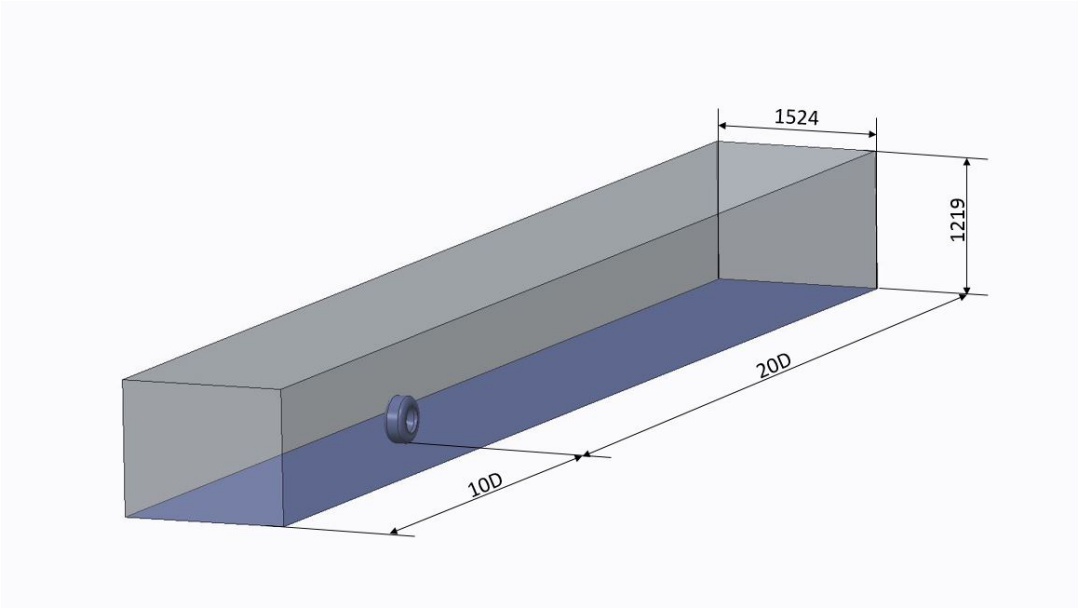

Figure 4.6: Fluid Domain complete with wheel. All dimensions in mm.

4.3.5.2 Meshing Strategy

For this investigation, an assembly meshing scheme was utilised. This is a Cartesian assembly method known as Cut Cell in ANSYS Meshing. The reason for using this method was because it provides two advantages. It was able to create high amounts of hexahedral cells around complex geometry greatly minimising the cell count and keeping most of the cells aligned to the flow direction when compared to an equivalent tetrahedral mesh. Another reason for

choosing this was that it was relatively simple to construct in comparison to fully structured block mesh. Given the complexity of the geometry and length of the project, a fully structured blocked mesh was not feasible and the Cartesian grid provided the best compromises for geometric accuracy, cell count, and high quality cells. A refinement zone was created in the domain to provide higher resolution in the near wake and around the wheel. The front of the refinement area was positioned 1.5D ahead of the centre of the wheel, the top of the refinement area was positioned 1D above the centre of the wheel and the rear face of the refinement area was positioned 4D behind the centre of the wheel. The width of the refinement box was 500mm full enclosing the wheel. This area was chosen so as to help capture the expected vortices and other flow structures which stem from various parts of the wheel.

The maximum cell size used on the face of the wheel was 2mm which grew out to 10mm inside the refinement area. After the refinement area the cell size grew to 50mm in the far field to the boundaries. An image of the resultant mesh used for a wheel with no camber or yaw angle is shown in Figure 4.7 below.

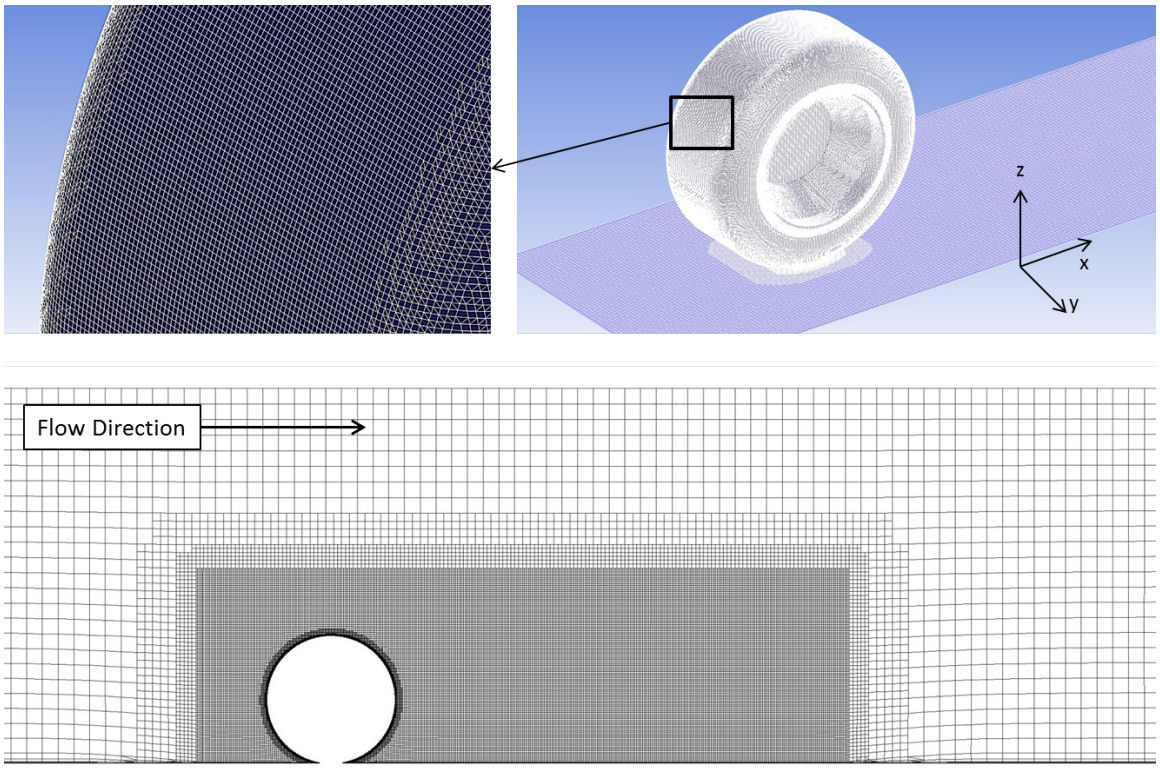

Figure 4.7: Final mesh used showing refinement zone and surface mesh on the wheel

One of the disadvantages of this meshing method was that as the assembly mesh grows, the increase in cell size is large. The volume change between boundaries is very sudden, and the cell size is effectively doubling in each direction. As a result the volume of the cell is increasing by a factor of 8.

To minimise this effect on the solution, the cells were kept as even as possible throughout the region surrounding the wheel. As the geometry around the wheel changes, the cell size inevitably had to change, however the resultant resolution around the wheel and cell size consistency was still far greater than what could be achieved using an unstructured approach, especially when one factors in the number of cells required. An inflation layer consisting of 10 layers around all of

the surfaces of the wheel and ground was created using two different methods. A first layer thickness of 0.01mm was used around all of the wheel surfaces with a growth rate of 1.2. A last aspect ratio approach was chosen for the road due to the large changes in cell size further away from the wheel itself. This forced the size of the last cell in the prism layer to depend on the cell in the domain immediately adjacent to it. A first cell height of 0.01mm was used again with the final aspect ratio of the last cell in the prism layer being set to 3. The growth rate of the cells from the first to the tenth layer was calculated automatically to ensure the aspect ratio control was met and to ensure the best overall mesh quality. For this investigation maximum y^+ values for all simulations were all below 1, therefore enhanced wall functions with enhanced pressure gradient effects were employed in the setup.

4.3.5.3 Boundary Conditions

The boundary conditions used for the simulations were consistent for all simulations. These are listed as follows:

- Inlet: Constant velocity inlet set at 18.6 m/s to match Fackrell's experimentation.
- Outlet: Constant pressure outlet set at 0 Pa gauge pressure
- Symmetry: A symmetry condition was used for the left, right and top sides of the fluid domain. This condition assumes the flow variables show

no variation along the symmetry direction. On the sides and top of the tunnel, this was assumed to be the case. This method also meant that a boundary layer mesh was not required which made the meshing process faster.

- Wall: Wall boundary conditions were applied to both the wheel and the ground. Moving wall conditions were applied to the ground and the wheel to match the airspeed. A translational condition was used for the ground moving at 18.6 m/s to match the inlet velocity and a rotational condition was used for the wheel rotating at 89.9 rad/s so that the velocity of the wheel also matches the velocity of the ground and freestream air.

These boundary conditions were kept consistent throughout the investigation. The only parameter which changed was the axis of rotation for the wheel when yaw angle was applied. Turbulence intensity and length scale at the inlet and outlet was calculated using $0.07 \times D$ [24, 33] where D is the wheel diameter. Therefore turbulence intensity was set to 2.9% and length scale was calculated and set to be 0.02912.

4.3.5.4 Solution Setup

For this analysis, a two stage solving approach was used. This approach involved gradually changing the solution once a number of iterations had been performed. This change introduced a higher order term to the solution equations which led to

a more accurate final solution. The stages involved first solving the model in first order for 500 iterations and then switching the model to solve in second order for an additional 7000 iterations. This method reduced the risk of early divergence and solution instabilities.

4.4 Summary

This chapter provided an overview of the methodology used for completing this research project. The fundamental flow equations which are used by the CFD software were described and a detailed breakdown of the computational model was shown. Furthermore, a detailed explanation of the various turbulence models was provided explaining their advantages and disadvantages.

A description of the Fackrell A2 wheel was provided and a full description of the computational methodology was discussed including the geometry creation, mesh generation, the boundary conditions used and the solution setup using ANSYS Fluent.

This method was followed for all simulations, the only variation was the geometry which was modified for the various camber and yaw angles tested.

5 Validation and Verification

This chapter discusses the various tests and comparisons performed to ensure the simulations provide accurate and reliable results. The various parameters investigated were the inlet and outlet boundary position, the number of cells in the inflation layer and the size of the grid. After performing the required steps to ensure the computational model was robust, the results obtained and validated against Fackrell's experiments for the A2 wheel. This wheel contained no camber and was not yawed. The simulation was compared using the lift and drag obtained and the pressure distribution over the wheel.

In addition to the computational model, the estimation of the percentage error has been discussed. This was estimated by considering the grid convergence index.

5.1 Grid Convergence Study

To ensure that the solution is independent of the size of the grid used, a grid convergence study was performed. An initial coarse mesh was created and run from which lift and drag data was gathered. Subsequently three further mesh refinements were performed and the percentage variation between simulations was calculated. The sizes of the grids used are shown in Table 5.1 below.

Table 5.1: Number of cells used for grid

Grid Tested	Number of cells (x10^6)
Coarse	3.9
Refinement 1	5.3
Refinement 2	9.2
Refinement 3	11.8

A graph was constructed showing the percentage variance is shown in Figure 5.1 below.

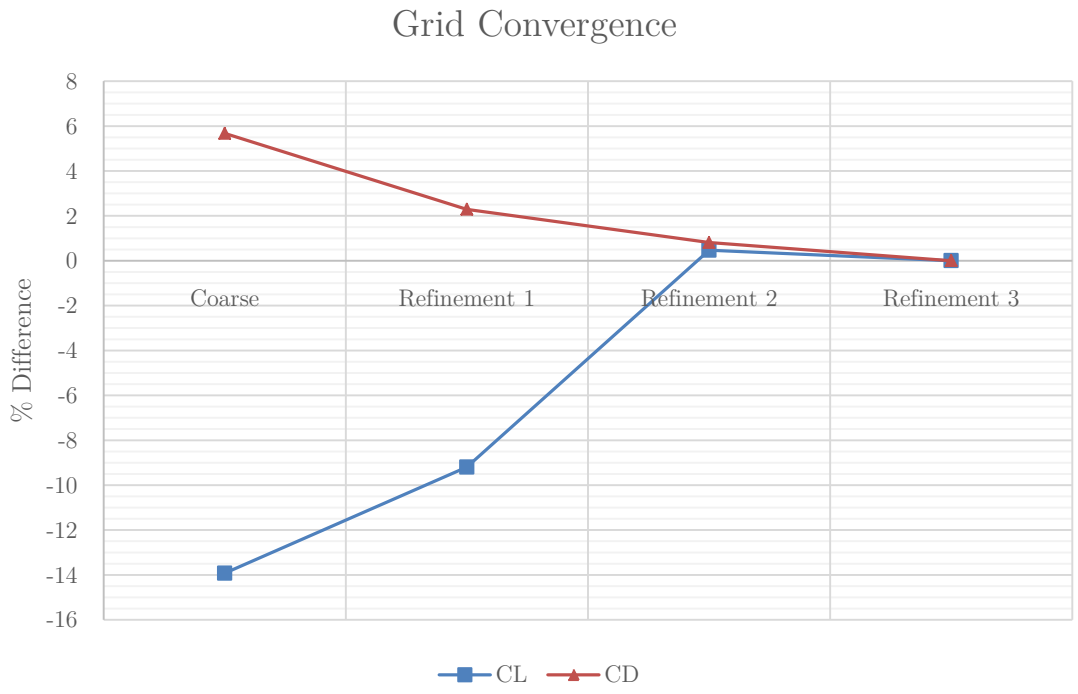

Figure 5.1: Grid Convergence Chart

From the graph above, it was observed that the variation in the lift and drag solution between the second and third grid refinements was below 1% and

therefore it was concluded that the solution was no longer dependant on grid size after refinement two. As a result of this, to be as computationally efficient as possible, the meshing parameters used for second refinement were used throughout this research.

5.1.1 Grid Convergence Index

To quantify the errors produced by the computational models, the grid convergence index (GCI) was used. The GCI was first proposed by Roache [38] and calculated an error using a selected value and selected mesh density in comparison to a theoretical asymptotic value. The GCI is calculated by first estimating an error and then multiplying this by a safety factor which is determined based on the number of mesh intervals being considered. The formulae used to calculate the GCI are shown below.

$$E_1 = \frac{r^p \epsilon}{r^p - 1} \qquad E_2 = \frac{\epsilon}{r^p - 1}$$

$$\epsilon = \frac{f_2 - f_1}{f_2} \qquad r = \frac{h_2}{h_1}$$

The value p is the order of convergence being used,f corresponds to the parameter being considered for the GCI, r is the ratio of grid characteristic lengths and subscripts 1 and 2 correspond to the coarser and find grids respectively.

GCI is then calculated using:

$$GCI_1 = F_S|E_1| \qquad GCI_2 = F_S|E_2|$$

Where the safety factor is denoted by F_S.

Using the data presented above, it was observed that the solution converged within 1% after mesh refinement two; therefore errors and the GCI were calculated refinement two and three. As only two grids are being compared, F_S was set to 3. Additionally, second order convergence was used for all solutions therefore p was set to 2 and for the two grids considered r = 1.28. The calculated errors and GCI for these two grids are shown in Table 5.2 below.

Table 5.2: Error and Grid Convergence Index for Lift and Drag Coefficient

	9.2 Million Elements		11.8 Million Elements	
	GCI	**Error**	**GCI**	**Error**
CL	0.04%	-0.01%	0.02%	-0.01%
CD	0.06	-0.02%	0.04%	-0.01%

It should be noted that the error values correspond to the error in only one direction, therefore only 50% of the total error. Based on the values calculated it was concluded that the mesh containing 9.2 million elements was sufficient. The added computational time of the finer grid did not improve the solution by any

significant margin. A maximum error of 0.04% was well within the accuracy required for this study.

5.2 Inlet and Outlet Position

In addition to grid convergence, the size of the fluid domain can also inadvertently affect the solution. The inlet and outlet boundaries need to be a sufficient distance away so as to ensure the flow can develop and stabilise. The most optimum model is the minimum inlet and outlet position needed such that the solution no longer changes. An initial large domain size was set and three inlet and outlet positions were tested. The upper and side boundaries can have an affect however these were selected and set to 1219 mm and 1524 mm respectively to replicate Fackrell's experiments and were not analysed in detail. The inlet and outlet positions tested are shown in Table 5.3 and Table 5.4 below. The distances are given in multiples of the wheel diameter from the centre of the wheel.

Table 5.3: Inlet Positions Tested

Inlet Position	Outlet Position
10D	20D
12D	20D
14D	20D
16D	20D

Table 5.4: Outlet Positions Tested

Inlet Position	Outlet Position
10D	20D
10D	22D
10D	24D
10D	26D

The lift and drag variation as the inlet and outlet positions were reduced was minimal as can be seen in Figure 5.2 and Figure 5.3 below.

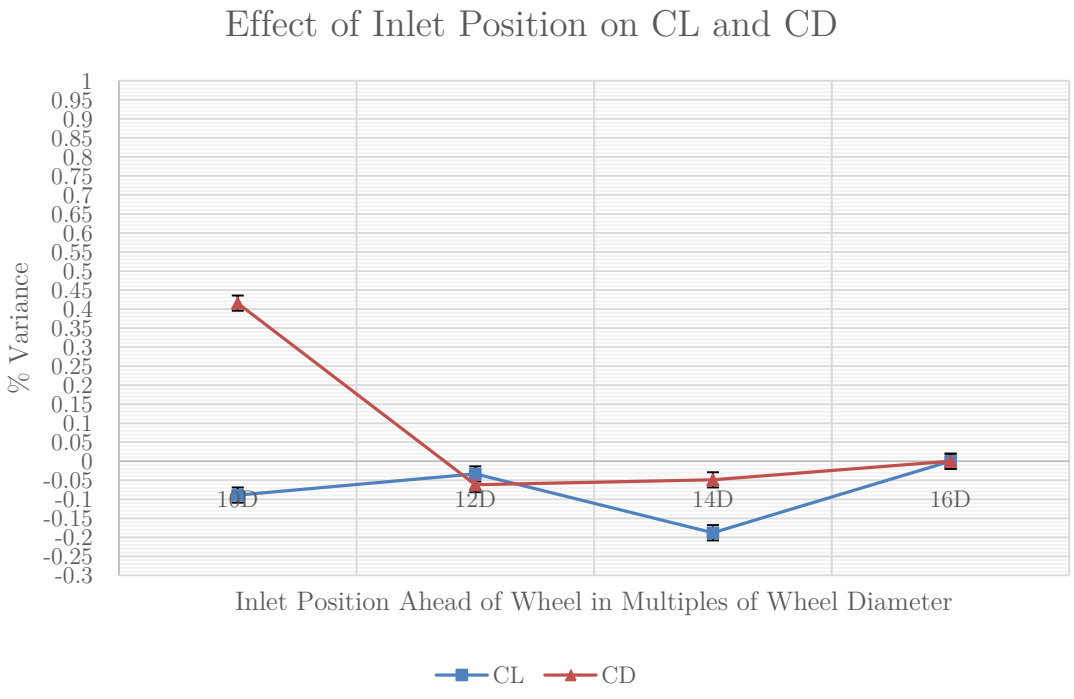

Figure 5.2: Effect of Inlet Position on the Coefficient of Lift and Drag. %Error for all Data ± 0.02%

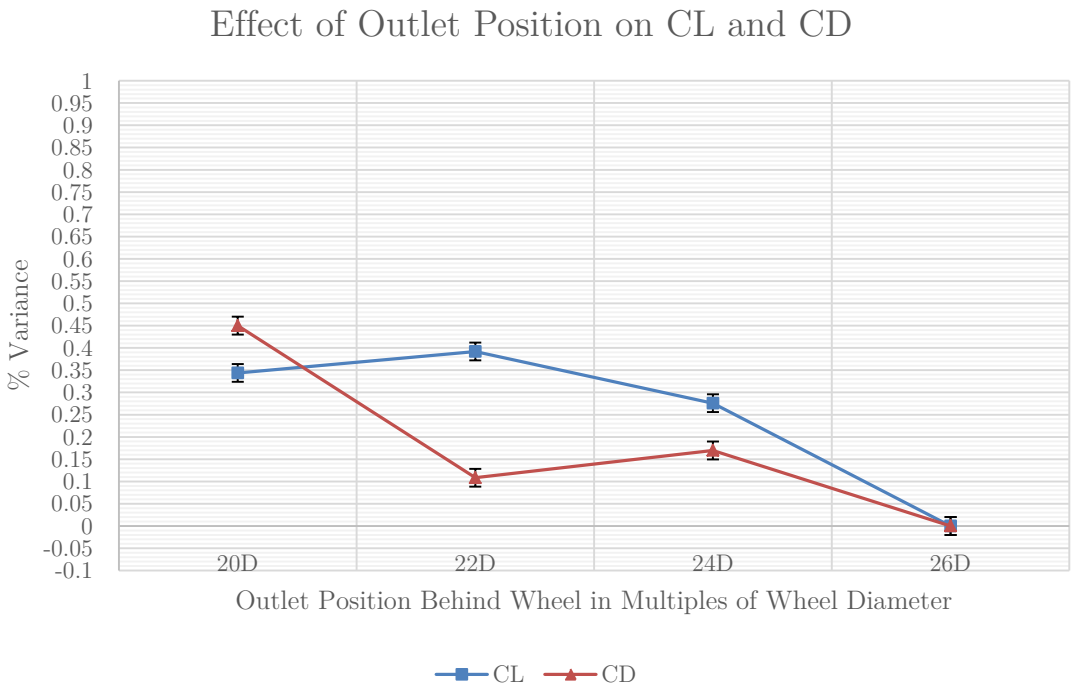

Figure 5.3: Effect of Outlet Position on the Coefficient of Lift and Drag. %Error for all Data ± 0.02%

From the charts presented above, it can be seen that the variation in lift and drag as a result of increasing the inlet and outlet position is less than 0.5%. As a result, for computational efficiency it was decided that all computational models have an inlet positioned 10D ahead of the centre of the wheel and an outlet positioned 20D behind the centre of the wheel.

5.3 Number of Cells in the Inflation layer

In order to model the boundary layer on a wall using CFD, an inflation layer must be created. The number of inflation layers used must be sufficient to capture the boundary layer profile, however in addition to this; the number of

layers used may have an influence on the final solution and must be investigated further. A number of inflation layers each consisting of a different number of cells were tested. The other mesh parameters were kept consisted using the settings obtained for the second mesh refinement. Inflation layers consisting of 5, 8, 10, 12 and 14 layers were tested. The resultant chart comparing the lift and drag is shown in Figure 5.4 below.

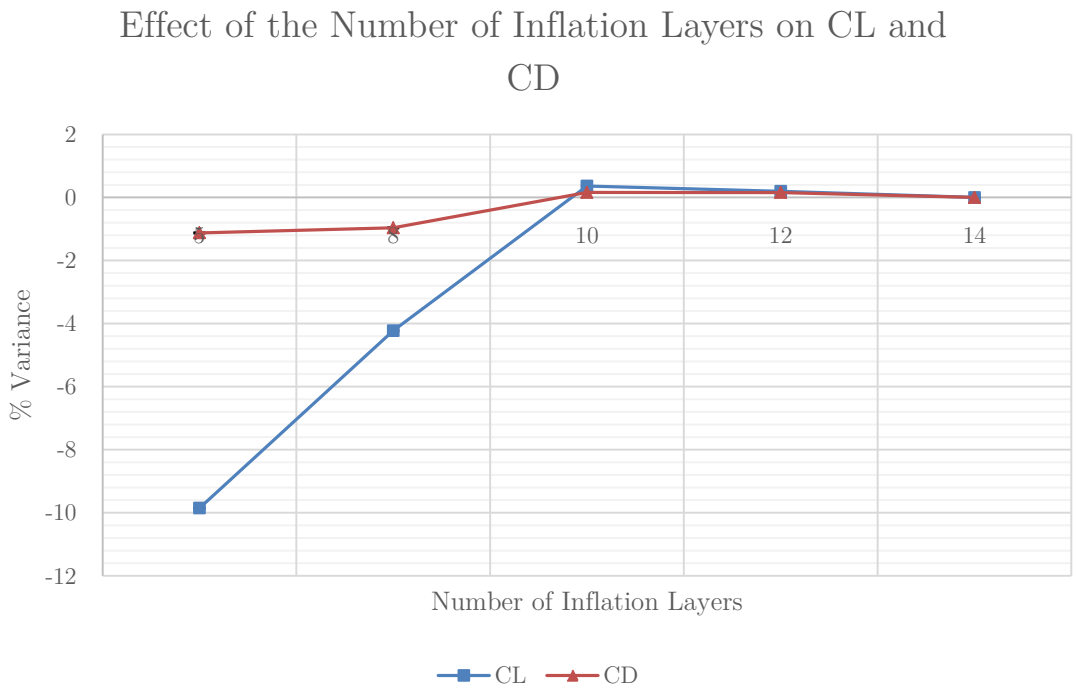

Figure 5.4: Effect of the Number of Inflation Layers on the Coefficient of Lift and Drag.

%Error for all Data ± 0.02%

From the graph above, it can be seen that after 10 inflation layers, the variance in lift and drag is very minimal and amounts to less than 1% difference. The 10 layers were also found to be sufficient to capture the height of the boundary layer

over the wheel and road and as such were used throughout this research. This can be seen in below.

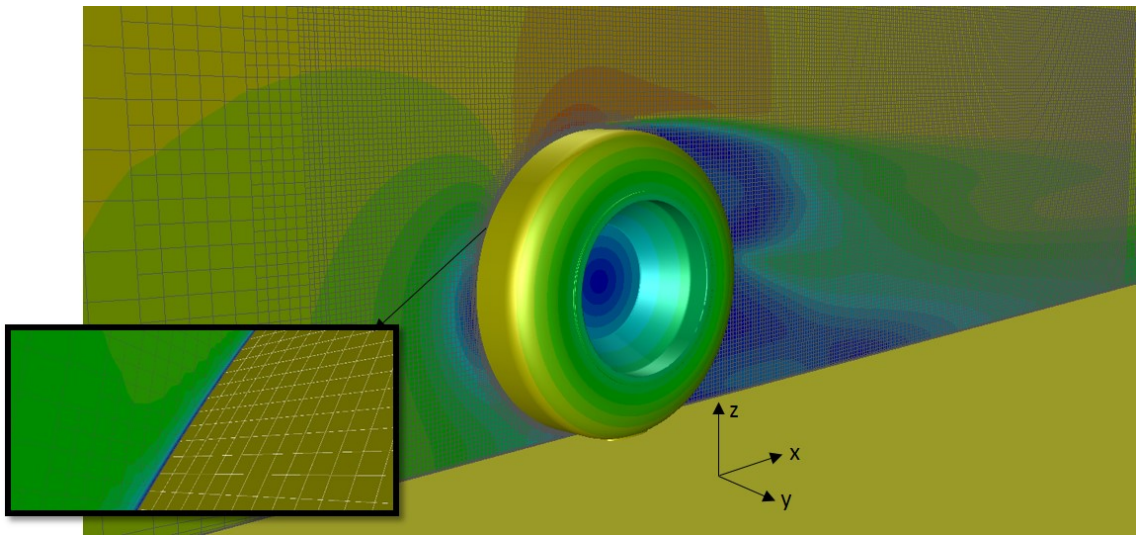

Figure 5.5: Contours of velocity magnitude with mesh overlay showing boundary layer flow.

The first cell height was set by considering the parameter y^+. For this study first cell heights were used such that all y^+ values did not exceed one. The first cell height of 0.01mm was set as a result of this. A y^+ below one allowed for the viscous sublayer could be modelled correctly.

5.4 Comparison to Fackrell

5.4.1 Lift and Drag

The lift and drag generated by the wheel was compared to the values observed by Fackrell. Various turbulence models were used to determine which most

accurately matches the experimental data. The lift and drag comparison is shown in Figure 5.6 below.

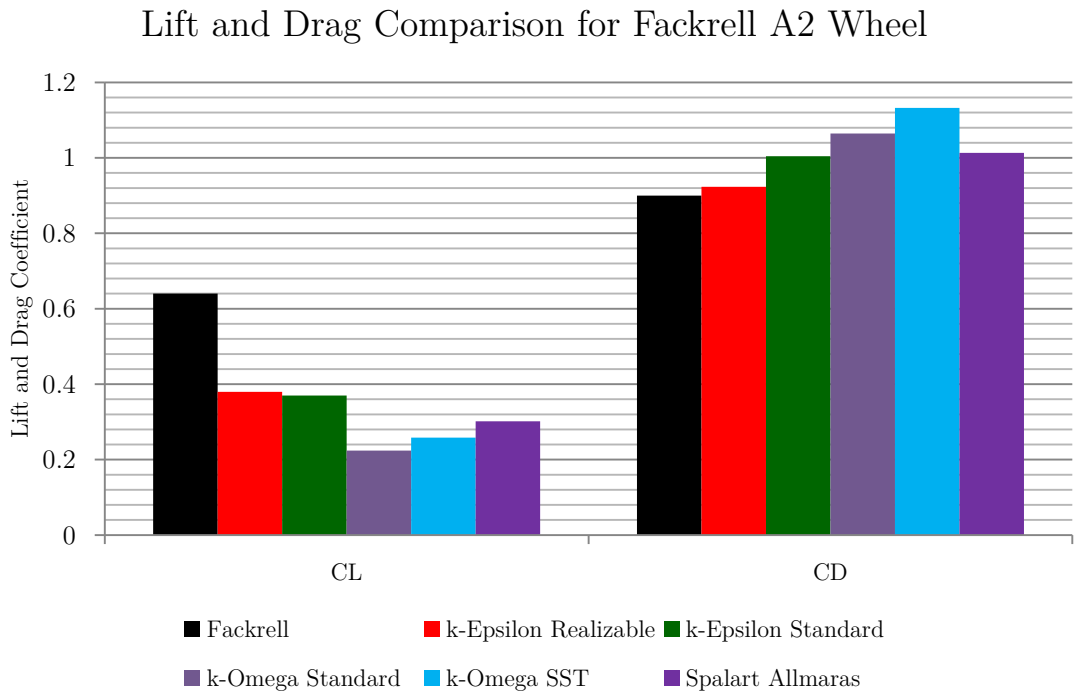

Figure 5.6: Lift and Drag Comparison comparing CFD to Fackrell. %Error for all CFD Data = ±0.02%

From the chart above, it can be seen that all the turbulence models, under predict the lift and over predict the drag generated by the Fackrell A2 wheel. However, the Realizable k-Epsilon turbulence model was shown to correlate the most to Fackrell's data. This was also observed in previous studies [14, 24, 26]. An unsteady transient approach would have been the optimum however due to time constraints and the computational resources required it was not possible. The reason for the large differences between turbulence models is fundamentally

down to their codes. Certain models such as the k-Omega models utilise parameters within its code which are advantageous for near wall and on surface flows, and therefore is able to model these features well however, in areas of high separation and vorticity this model does not perform well at all [35]. This resulted in predictions for lift and drag which were far from the experimental data. Drag in particular was highly over predicted.

The k-Omega SST model, proved to be a great improvement over the standard model however, the predictions for lift and drag were still far from the experimental data. The improvements made to the realizable version of the k-Epsilon model meant that the flow in the boundary layer and in the wake region was modelled far better than both k-Omega models.

The Spalart-Allmaras one equation model was tested primarily to see how different the results would be compared to the more advanced models. The one equation model is computationally extremely efficient and as such if the results did not vary significantly the reduced simulation time would have been very beneficial. However as expected the flow was difficult to resolve using the one equation model and as such the lift and drag forces were not predicted well.

The standard k-Epsilon model performed quite well however, its limitations are the opposite to that of k-omega. This model does not perform well with on surface

flows as mentioned in the previous chapter. As expected, the drag and lift forced predicted were more realistic compared to the standard k-omega however the predictions were not as good as the realizable k-Epsilon variant.

5.4.2 Pressure Distribution over the A2 Wheel

In addition to the lift and drag results, the coefficient of static pressure over the centreline of the wheel was used to provide an understanding of how well the CFD models were able to predict the on surface flow features of the wheel. A comparison chart is shown in Figure 5.7 on the following page.

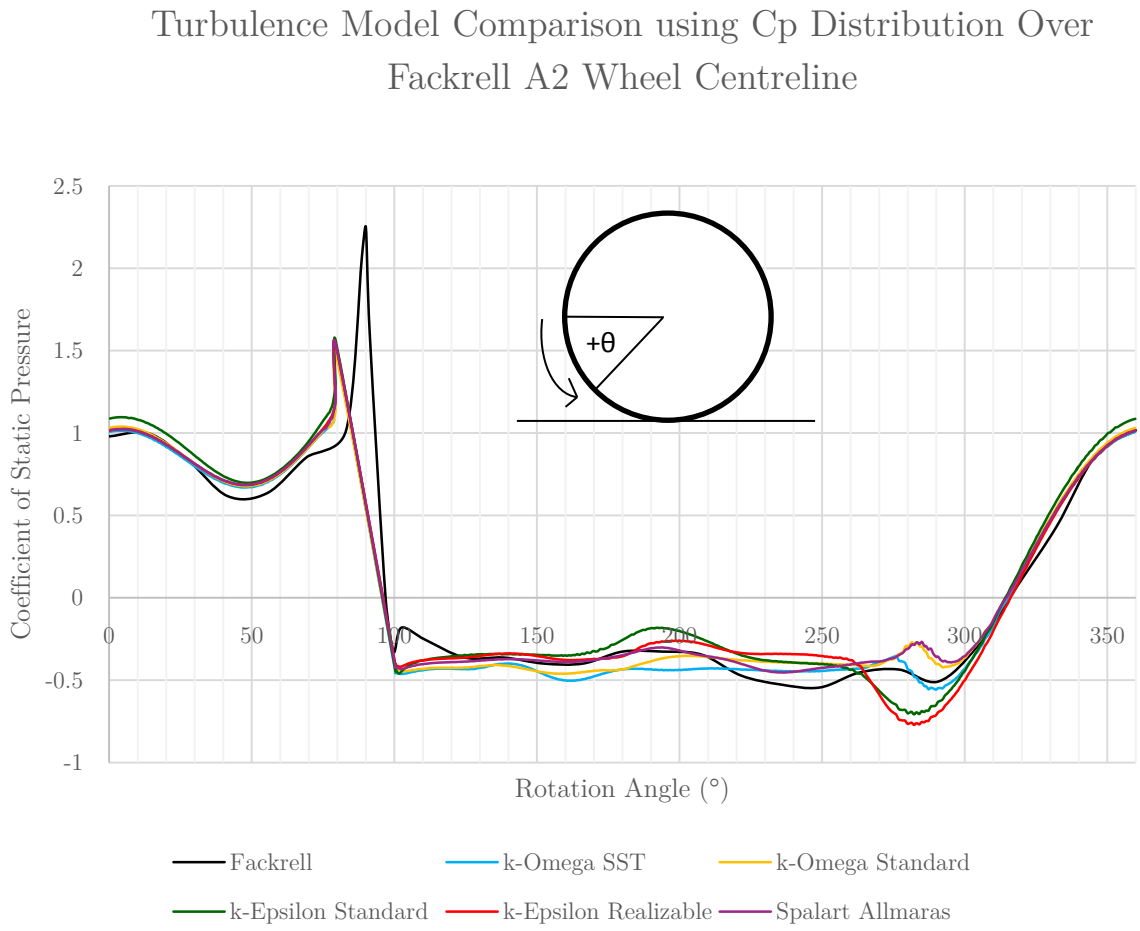

Figure 5.7: Cp Distribution over Fackrell A2 Wheel Centreline - Turbulence Model Comparison. %Error for all CFD data = ±0.02%

From Figure 5.7, it can be seen that the trends displayed by the CFD results do align quite well to what was observed by Fackrell. There are areas of the curve which do not align, in particular the large positive pressure peak at the contact patch.

The reason for this discrepancy is how the contact patch was modelled. In order to simulate a contact patch, the wheel was partially sunk into the ground. As such there was an area on the wheel where no data was calculated in the solution.

This region was located between 75 degrees and 100 degrees and corresponds to the region of contact with the road itself. It was not possible to model two separate surfaces intersecting and sliding on each other as the meshing process would not allow this. Prism layers meshing between two tangential surfaces would result in highly skewed cells [24, 33, 34]. Fackrell discussed that at least 30% of the lift generated by the wheel was generated by the area between 70 degrees and 90 degrees on the wheel [4]. As the CFD model did not have this data available, the curves do not align in this area.

However it can be seen that as the angle increases towards the front of the contact patch, the pressure peak is increasing rapidly showing that if the data required was available the CFD would have predicted a similar result. Over the rear side of the wheel, behind the contact patch, and at the separation point, it was observed that the CFD models closely matched the data produced by Fackrell.

Comparing the turbulence models used, it was observed that they all show similar behaviour over the wheel, however some discrepancies can be seen behind the contact patch and at the separation point. The k-Epsilon models show a larger negative pressure peak in comparison to the other models. The location of the separation point however, is quite consistent across models and aligns quite

reasonably with Fackrell's work. Fackrell described the separation point being located in a region between 270-290 degrees on the top surface of the wheel [4].

Based on this trend along with the trends shown over the remainder of the wheel, it was concluded that the CFD method and data was robust enough to use for further investigations. When comparing the turbulence models it was observed that the models that have been optimised for near wall flows were able to produce very accurate predictions when compared to Fackrell, most notably, the k-Omega SST mode which showed great performance near the separation point. However as mentioned previously, this model did not predict the lift and drag very well, therefore this was not the model of choice.

From the information generated, it was concluded that the Realizable k-Epsilon turbulence model would be used throughout the research. This model showed good correlation to Fackrell's data at the stagnation point and towards the front of the contact patch, it showed reasonable correlation over the rear of the wheel and behind the contact patch and also predicted the location of the separation point accurately within the range described by Fackrell. In addition to this, the model produced the best prediction of lift and drag as seen in Section 5.4.1.

5.5 Summary

After performing a series of simulations it was concluded that for this investigation the following grid, fluid domain and turbulence parameters were to be used.

- Optimum grid size: 9.2 million elements
- Inlet Position: 10D ahead of the centre of the wheel
- Outlet Position: 20D behind the centre of the wheel
- Turbulence model to be used throughout: k-epsilon Realizable

Additionally, the positions of the top and side boundaries of the domain were set so as to mirror the cross section of the wind tunnel used by Fackrell [4].

6 Results and Discussion

6.1 Effect of Camber Angle

6.1.1 Lift and Drag

The variations in lift and drag observed for a cambered wheel displayed an interesting trend. A comparison chart showing the lift and drag variation is shown in Figure 6.1 below.

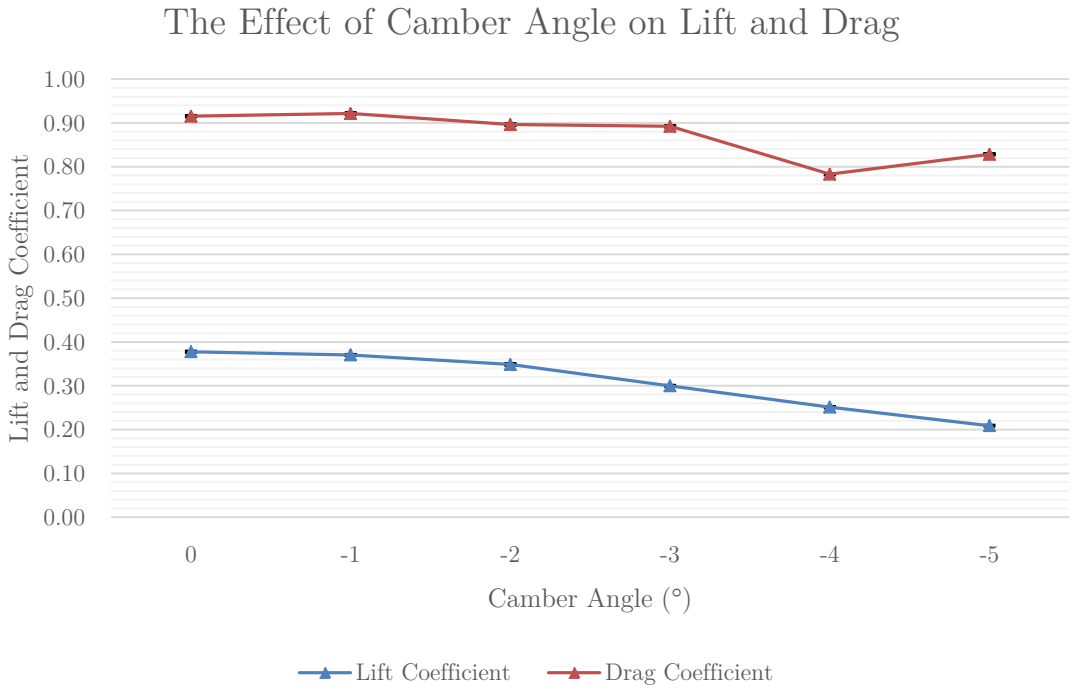

Figure 6.1: Lift and Drag Comparison – Camber. % Error for all data = ± 0.02%

From Figure 6.1 it was observed that as higher levels of camber are applied to the wheel, the lift force steadily reduced. A reason for the reduction in lift is the fact

that due to the applied camber, the height between the outboard side of the wheel shoulder relative to the ground is increasing, allowing more air to flow through the gap. This has an effect on the level of pressure at the contact patch and on the lower portion of the wheel. The flow near the boundaries of the wheel and the road are interacting in a different manner. The region which experiences stagnated flow is reduced and this will further contribute to the reduction in lift experienced.

The drag force remained relatively consistent up until negative four degrees where a sharp decrease in drag was observed. After this the drag value remained close to this level at negative five degrees. A reason for this variation was that it was due to the overall shape of the contact patch. As higher amounts of camber were applied, the contact patch began to taper as mentioned in the previous section. From zero to negative three degrees camber, the drag force did not change by more than 2.5% and the contact patch shape did not change significantly and still consisted of four edges.

Negative four degrees of camber was the point at which the contact patch changed the most. At this point the contact patch changed from a trapezoidal shape to triangular shape consisting of only three edges. This significantly affected how the airflow moved around the contact patch and the front section of the wheel shoulder. From negative three to negative four degrees the drag force

varied by 12.2%. This large reduction in drag at negative four degrees was also observed by Knowles [13] as mentioned in Section 2.2.2

The results for lift and drag show that the camber angle has a much larger impact on the lift produced compared to the drag. Over the entire range tested, the maximum variation in lift was 44.7% compared to only 14.5% for drag. The trend for lift is expected to continue regardless of any further variations to contact patch shape. At even greater levels of camber, it is expected that the drag force should remain consistent until another significant variation to the contact patch shape was to be observed.

6.1.2 Effect of the Contact Patch Shape

Investigating variations in the contact patch shape was an integral part of this research. The contact patch shape was changed as the wheel was cambered. The original contact patch shape was essentially rectangular with curves at the corners. As the wheel was cambered, the contact patch started to taper towards the outboard side of the wheel.

It was observed that as the camber angle increased to negative three degrees the taper steadily increased and that the contact patch shape consisted of four straight edges and four corners. However, at negative four degrees camber and higher, it was observed that the contact patch was no longer a rectangular shape

and instead became triangular. The variations in the contact patch are shown in Figure 6.2 below.

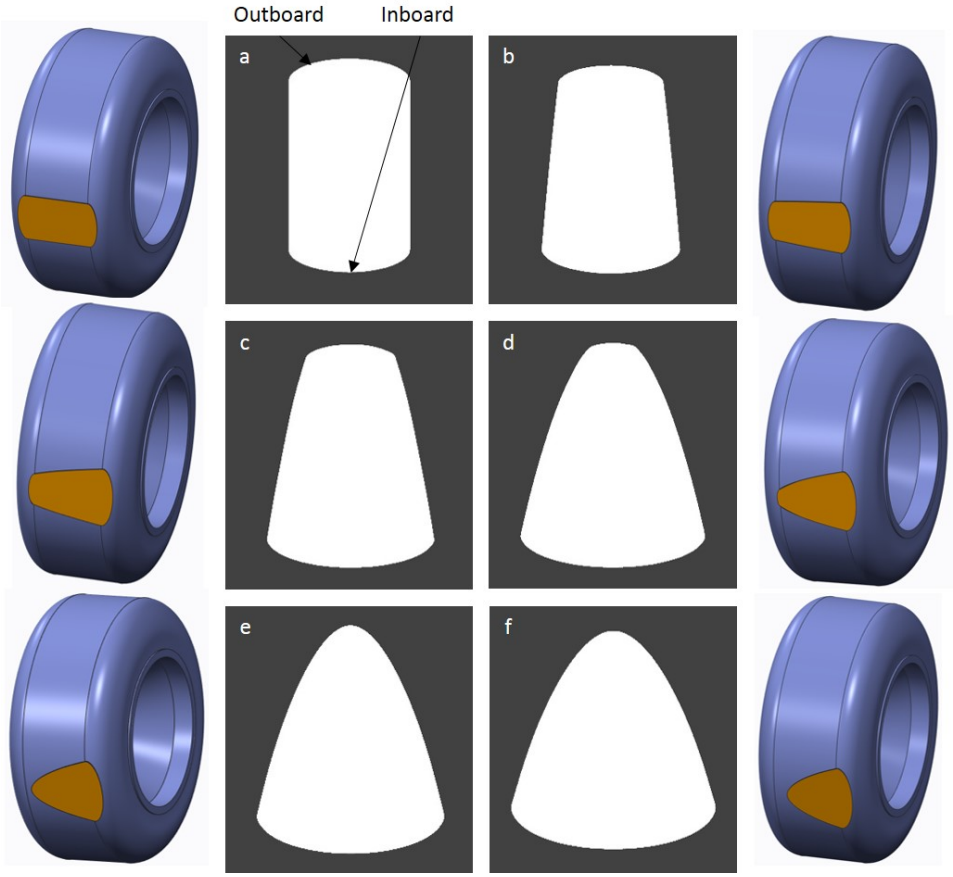

Figure 6.2: Contact patch variation due to camber angle. a) 0° b) -1° c) -2° d) -3° e) -4° f) -5°

As the contact patch varied, the behaviour of the flow around the contact patch also inevitably changed. To compare and visualise the flow around the contact patch, a slice was taken through the mid-plane of the contact patch and contours of total pressure coefficient were plotted. This is shown in Figure 6.3 on the following page.

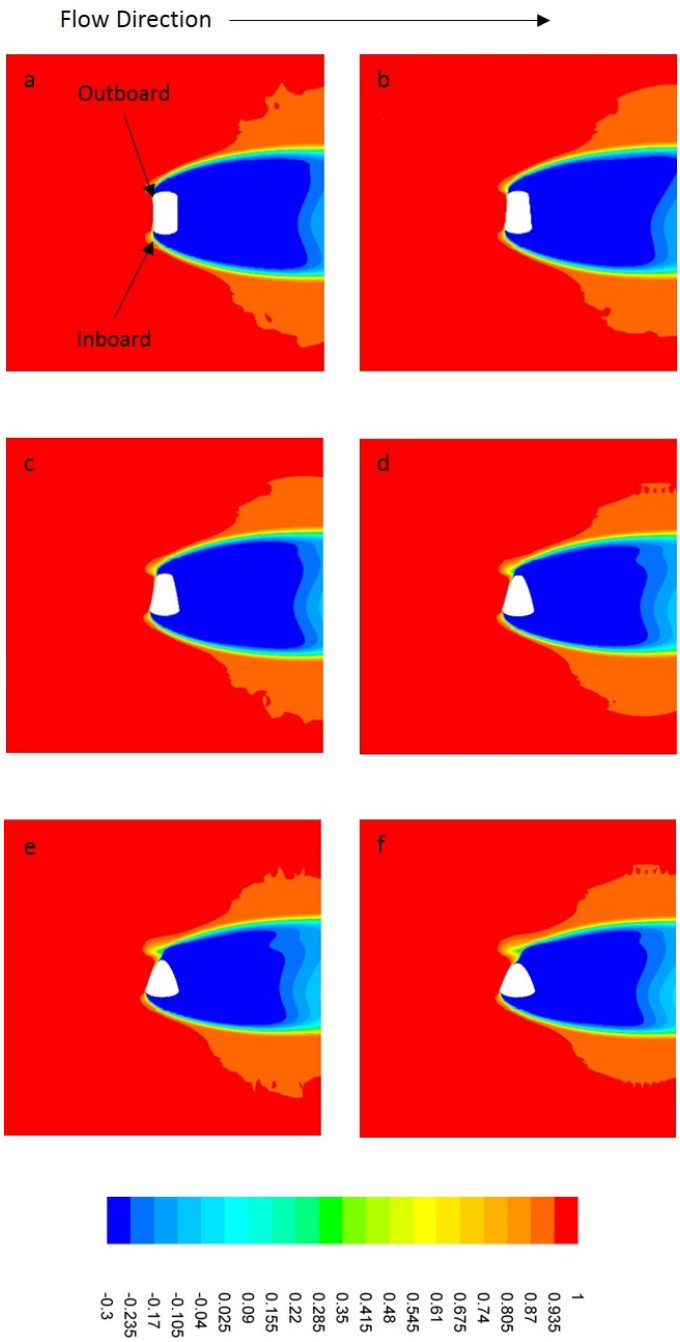

Figure 6.3: Contours of Total Pressure Coefficient at the mid plane of the contact patch – Camber a) 0° b) -1° c) -2° d) -3° e) -4° f) -5°

After comparing contour plots of total pressure coefficient located at the mid plane of the contact patch, it was observed that the flow behind the contact patch started to skew towards the tapering side. At higher camber angles the

variation in the flow became more evident, however once the flow moved past the contact patch, a common shape was observed. The flow is affected the most at the contact patch itself and not as significantly downstream.

In addition to this skewness, it was observed that the shape of the contact patch had a significant impact on the formation of the jetting vortices which formed from the leading edge of the contact patch. It was observed that as the contact patch tapers, the formation of the jetting vortex on the outboard side is moved rearward with the leading edge of the contact patch. This distance rearward predominantly corresponded to the amount of taper of the contact patch. At higher camber angles when the contact patch where no leading or trailing edge is present the jetting vortex was observed to stem from the cusp of the contact patch. This is discussed in more detail in Section 6.1.4.

6.1.3 Pressure Distribution over the Wheel

Given that the addition of camber angle had a significant effect on the overall lift and drag on the wheel, it was important to identify the areas of the wheel which were contributing to this. To do this the coefficient of static pressure was plotted over the centreline of the wheels. This is shown in Figure 6.4 on the following page.

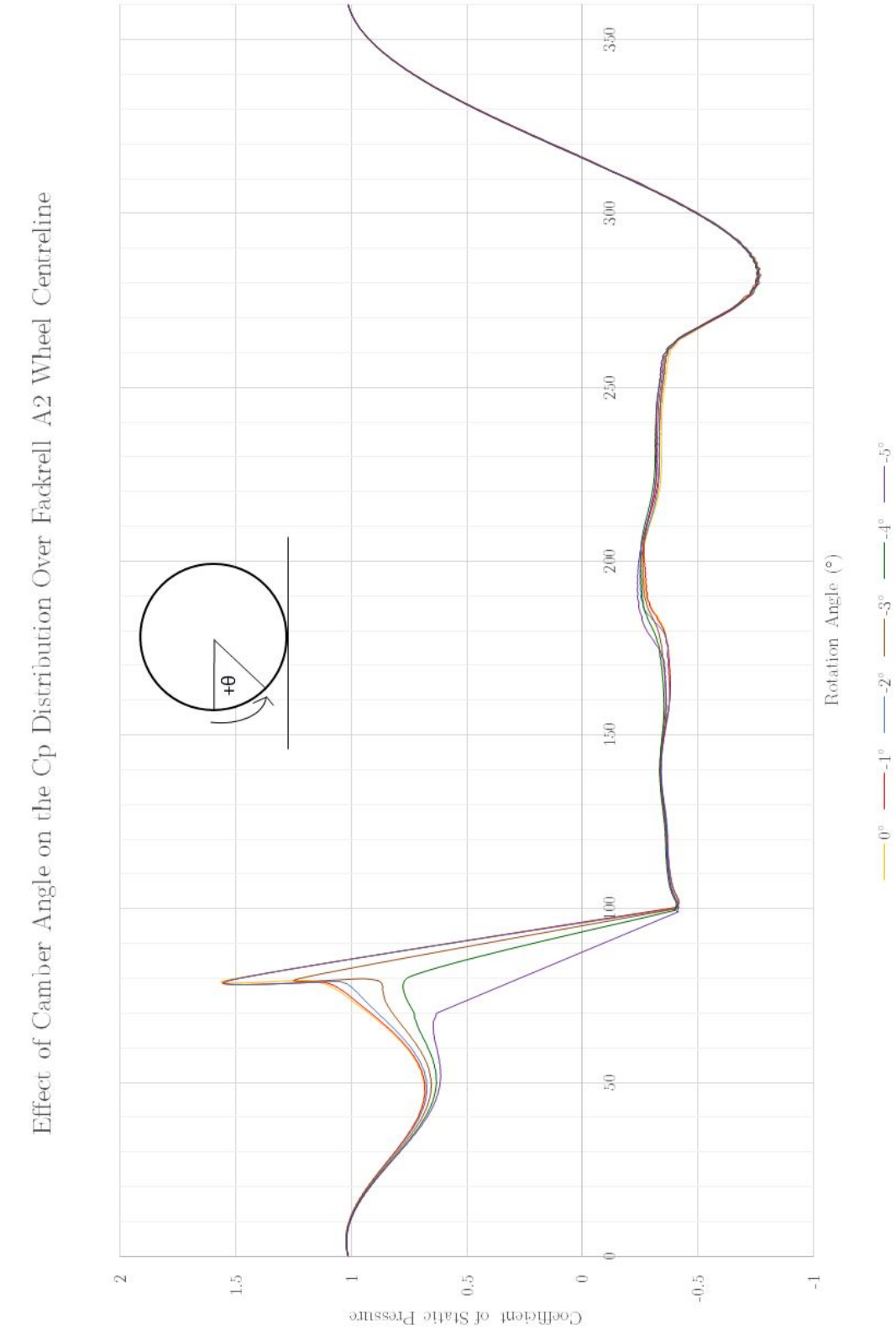

Figure 6.4: Comparison of Static Pressure Coefficient over wheel centreline – Camber. %Error for all data ± 0.02%

From Figure 6.4, it can be seen that a key area of interest is the area from the stagnation point on the front of the wheel to the contact patch. Behind the contact patch slight variations were observed however these pressure variations are very small. The top surface of the wheel showed no variations due to the camber angle. The separation point on the wheel did not change and it can be concluded that the separation over the wheel did not contribute to the variations in lift and drag.

From the stagnation point to the contact patch, it was observed that as camber was increased, the positive pressure peak steadily reduced, being completely eliminated at five degrees. This confirms what was discussed earlier which shows that as the wheel is cambered the extra area the flow has to move around the contact patch drastically affects the interaction between the wheel and the road. It was be seen that as the wheel is cambered there is less compression of the flow ahead of the contact patch leading to a reduction in the positive pressure peak.

As mentioned in previous sections, the start of the outboard jetting vortex was delayed due to the shape of the contact patch tapering. Previous literature has shown that this jetting flow forms as a result of this flow compression between the wheel and the road and therefore is not surprising that the peak is reduced. This is discussed further in the following section. The observation of a lower pressure peak agreed well with the reduction in lift observed earlier. Should the

camber angle be increased further it is speculated that the initial positive pressure peak would continue to reduce further until a point where further angles will not affect the flow ahead of the contact patch. Rather it is speculated that at this point, the flow on other regions of the wheel would start to change.

6.1.4 Effect of Camber on the Flow Structures around the Wheel

As mentioned earlier, the shape of the contact patch had a predominant effect on the formation of the jetting vortices around the wheel. The effect of the tapering contact patch on these vortices can easily be visualised through the use of constant velocity iso-surfaces and by visualising the flow at the centre plane of the wheel. A number of other flow features were also observed around the wheel. A comparison of three angles is shown in Figure 6.5 on the following page.

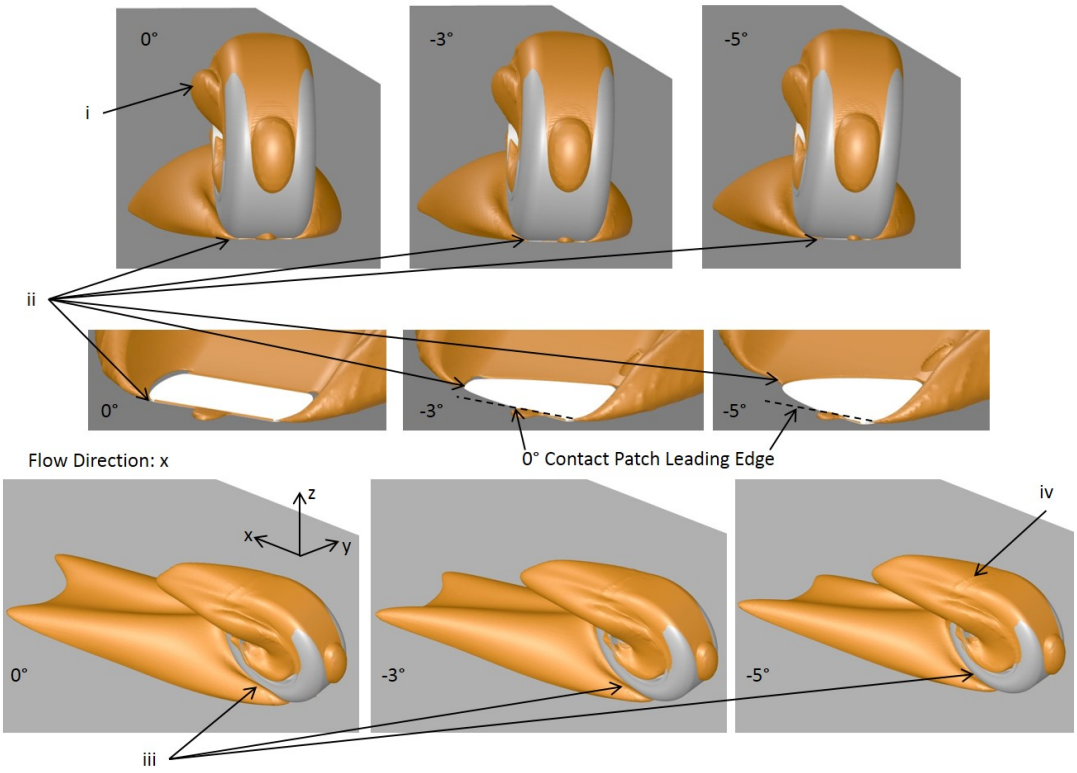

Figure 6.5: Flow structures around cambered wheel. i) Rim vortex ii) Outboard jetting vortex formation point at tapered contact patch iii) Variations in length of the outboard jetting vortex from wheel shoulder iv) Recirculation region due to separation over the wheel.

From the figure above, the main flow features around the rotating wheel and the key variations due to camber can be observed. The single rim vortex (i) was due to an increased width on one side of the wheel rim. At the contact patch (ii) the variations to the formation point of the jetting vortices were observed. The formation point was observed to move rearward and further toward the centre of the wheel underneath the wheel shoulder as the angle increased and this caused the outboard jetting vortex to behave differently when moving around the lower wheel shoulder (iii). It was observed that this jetting vortex did not interact with

the wheel shoulder in the same manner as the camber was increased. A larger area of the wheel shoulder was exposed as the camber increased. Finally, a large recirculation region was present behind the upper portion of the wheel and was consistent for all models (iv).

To compare how the formation point of the outboard jetting vortex was moving rearward, contours of total pressure coefficient were plotted at the origin. This centre plane was located at x/D = 0 and is shown in Figure 6.6 below.

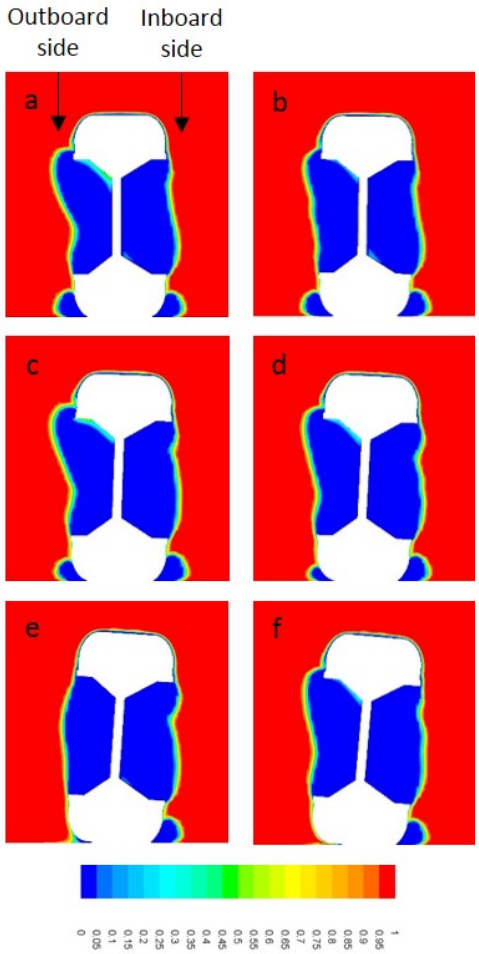

Figure 6.6: Contours of Total Pressure Coefficient at x/D = 0 – Camber. a) 0° b) -1° c) -2° d) -3° e) -4° f) -5°

From Figure 6.6, the effect of the tapering contact patch is clear. At this location, the size of the outboard vortex steadily reduces as the camber angle increases showing that the vortex was not developed to the same level. Once camber reached negative five degrees, the vortex cannot be seen which suggests that the vortex has formed at a location behind the centre plane of the wheel. This vortex in fact stems from exactly x/D = 0. Other flow features in this plane remained unaffected. The inboard vortex was not observed to be affected at all. An additional plot showing a velocity comparison in the centre plane is shown in Appendix A.

This delay in the formation of the outboard jetting vortex was a key feature and it was shown to have a large effect on the flow downstream of the wheel. To observe the effects of this, contours of total pressure were plotted at locations, including a point in the wake immediately behind the wheel at x/D = 0.52, and two points further downstream at x/D =0.84 and x/D = 1.42. These are shown and discussed in the following pages.

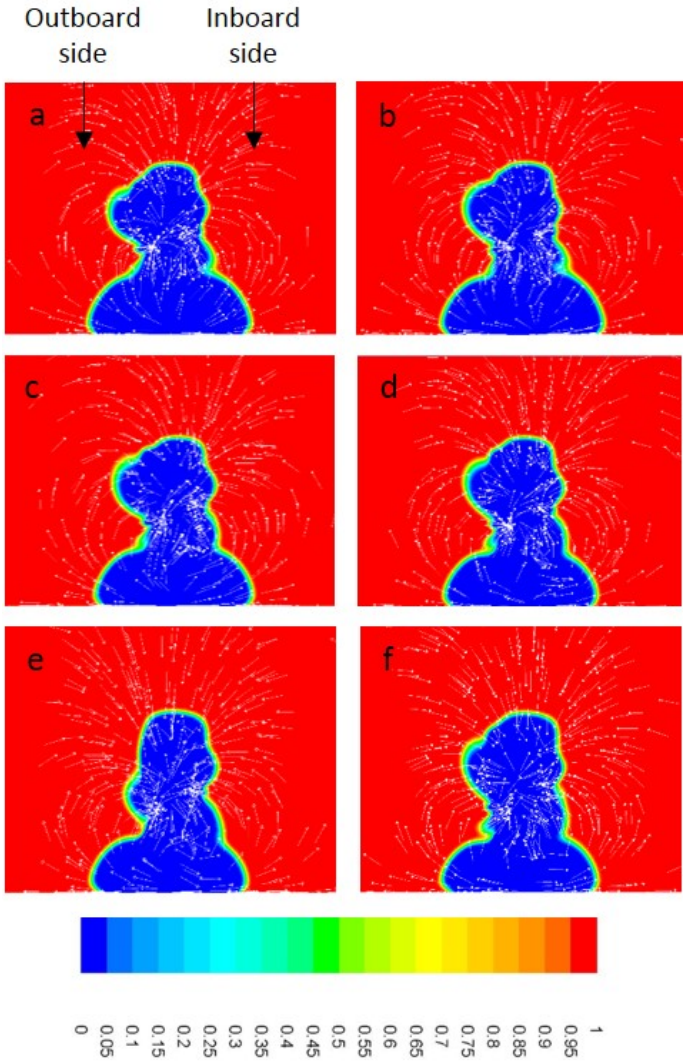

Figure 6.7: Contours of Total Pressure Coefficient located at x/D = 0.52 – Camber. a) 0° b) -1° c) -2° d) -3° e) -4° f) -5°

From Figure 6.7, it can be seen that immediately behind the wheel the flow characteristics and overall shape of the wake does not change significantly as a result of a change in camber. One variation was that the vortex which starts to form at the outboard side of the rim in the negative four degrees simulation was shown to be located slightly lower down compared to the other angles and may be attributed to the RANS approximation of the simulation however further

investigation is required to confirm or deny this. In reality is expected that the flow structures at this location would mimic the other camber angles.

A key observation at this location was that as the camber angle increased, the outboard jetting vortex was larger than the inboard vortex for all angles apart from zero and negative one. This can be attributed to the delayed formation of the outboard vortex as expected. This delay has meant that the outboard vortex contained more energy and is able to maintain its size and strength for longer in comparison to the inboard vortex. Negative one degrees of camber did affect the outboard jetting vortex in a similar manner to the others however the variation at the contact patch was not significant enough to show any large variations to the wake at this location.

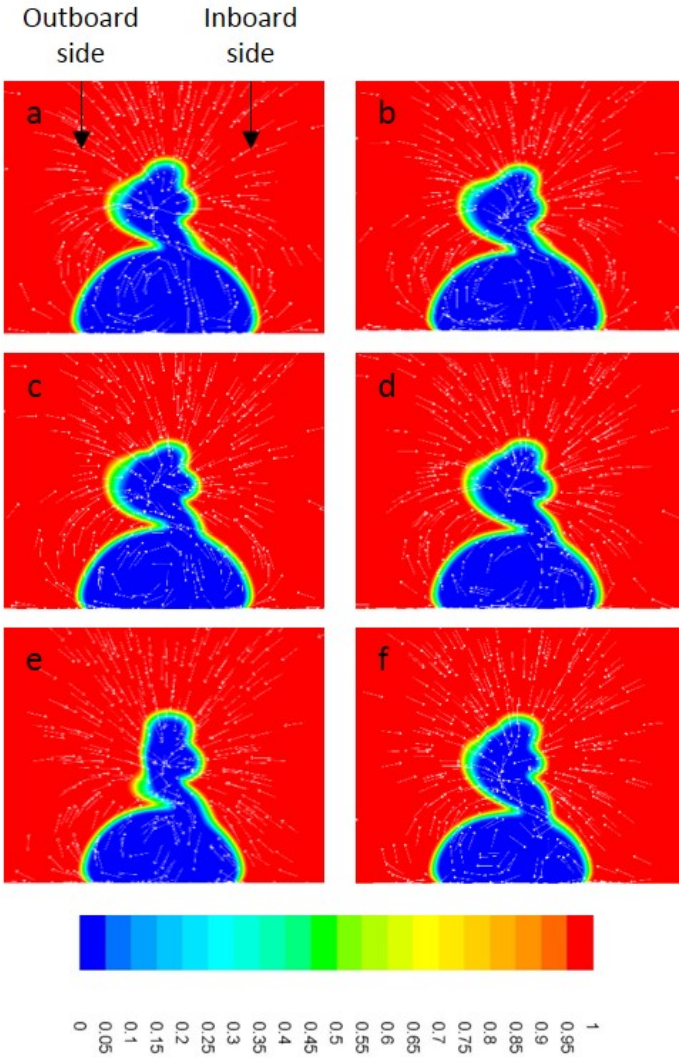

Figure 6.8: Contours of Total Pressure Coefficient located at x/D = 0.84 – Camber. a) 0° b) -1° c) -2° d) -3° e) -4° f) -5°

From Figure 6.8 above, a similar trend to the previous location was present. The flow structures were observed to remain consistent across the range of camber angles, aside from the profile negative four degrees due to the approximation of the vortex location being different. At this location, it can be observed that the outboard jetting vortex still dominates as the camber is increased and that the upper section of the wake is much thinner. The flow behind the centre of the

wheel was also observed the skew to one side. This shift can be attributed to the interaction of the flow at this location with the outboard jetting vortex. Additionally, the disturbances to the flow due to the separation point over the wheel are reduced at this location and it is the vortical flow structures which are primarily maintained.

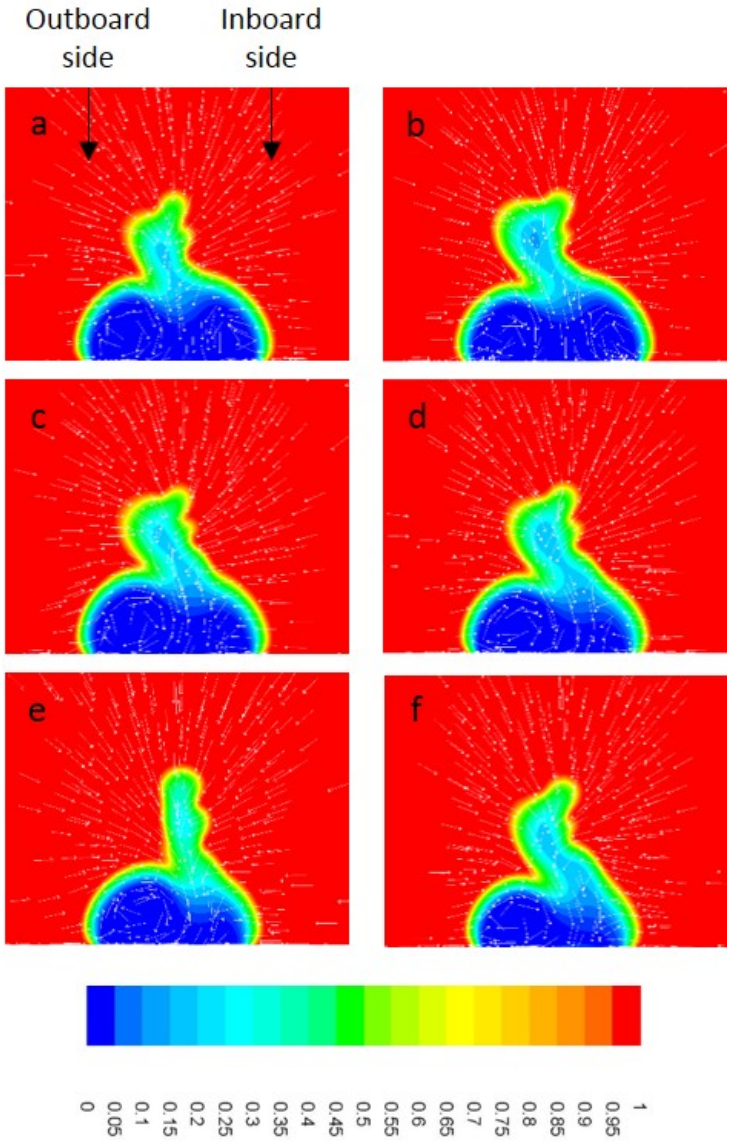

Figure 6.9: Contours of Total Pressure Coefficient located at x/D = 1.42 – Camber. a) 0° b) -1° c) -2° d) -3° e) -4° f) -5°

At the flow moves further downstream to x/D = 1.42 in Figure 6.9, the flow structures have not been observed to change. The energy within the flow structures has been observed to reduce and their impact on the overall flow is shown to have reduced however the outboard jetting vortex is still very strong. As the camber increased, the energy within the smaller vortices and areas behind the centre of the wheel has significantly reduced. The skewed nature of the flow was also observed at this location. The inboard jetting vortex had also deteriorated far more in comparison to the outboard jetting vortex.

From the observations made, it is apparent that camber has a much larger effect on the flow very close to the wheel in comparison to the further downstream in the wake region. The major variations to the flow have all stemmed from the contact patch and any downstream effects are as a result of this. The vortex which forms from the outboard side of the contact patch was shown to maintain its strength for a longer duration and extended further into the wake compared to the inboard jetting vortex. At the wheel, these variations resulted in the lift and drag forces changing at each angle.

6.2 Effect of Yaw Angle

6.2.1 Lift and Drag

The lift and drag produced by adding yaw to the wheel showed a completely different trend when compared to camber. It was observed that as the yaw angle increased, the lift and drag both steadily increased. At high yaw angles above 15 degrees, lift was observed to increase as per the trend however drag increased at a much higher rate. A comparison chart showing the effect of yaw on lift and drag is shown in Figure 6.10 below.

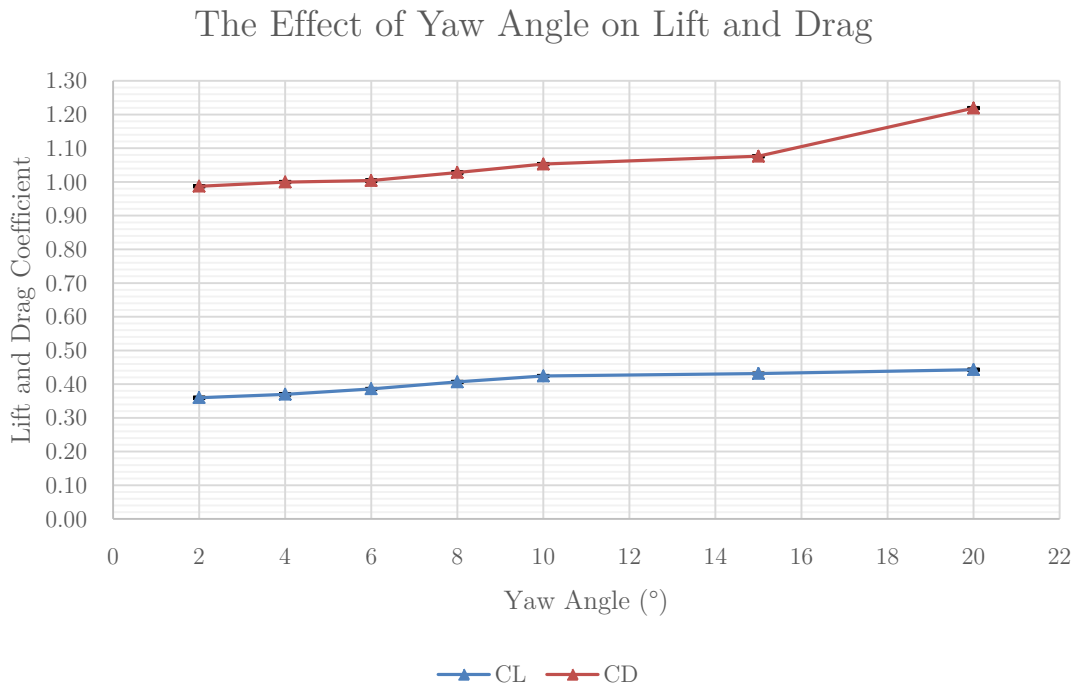

Figure 6.10: Lift and Drag Comparison – Yaw. % Error for all data = ± 0.02%

The increase in lift can be attributed to the fact that as the yaw increased the separation of the flow at the front of the contact patch reduces, as shown earlier. This resulted in the flow remaining attached to a larger surface of the wheel. Additionally as yaw increased, the internal surfaces of the wheel rim became exposed to the flow, resulting in new lifting surfaces being exposed from the wheel. Above 10 degrees these two changes did not show any significant increase in the lift. From 10 to 20 degrees the lift was shown to increase by only 4.4% compared to 17.9% from two to 10 degrees. The drag however, steadily increased up till 15 degrees and a shape increase was observed at 20 degrees. The drag increased steadily as the frontal area of the wheel exposed to the flow increased. At extreme yaw angles above 15 degrees, it was shown that the drag increases drastically. From two to 10 degrees the drag increased by 4.9% however, from 10 to 20 degrees this increase was 15.8%. This was a direct result of the flow changing drastically in the wake. This is shown in more detail in Section 6.2.4, however the increased area exposed to the flow resulted in variations to the recirculation regions around the rear of the wheel creating larger areas of turbulence. It was also observed that as the wheel was yawed, the rear portions of the wheel were more exposed to incoming flow and therefore the flow structures directly behind the wheel contained more energy resulting in longer sustained disturbances to the flow. This is discussed and can be observed further in Section

6.2.4. As a result it was not surprising that an increase of this magnitude in drag and drag was present given the large yaw.

6.2.2 Effect of the Contact Patch Shape

The contact patch had a different effect on the flow around the wheel when compared to camber. The shape of the contact patch remained constant however its alignment to the flow varied due to the applied yaw. At the base of the wheel this affected both the outboard and inboard jetting vortices. The introduced yaw decreased the angle of the flow separating from the outboard side of the contact patch and increased the angle on the inboard side. To visualise this, contours of total pressure coefficient were similarly plotted through the mid plane of the contact patch and is shown in Figure 6.11 on the following page.

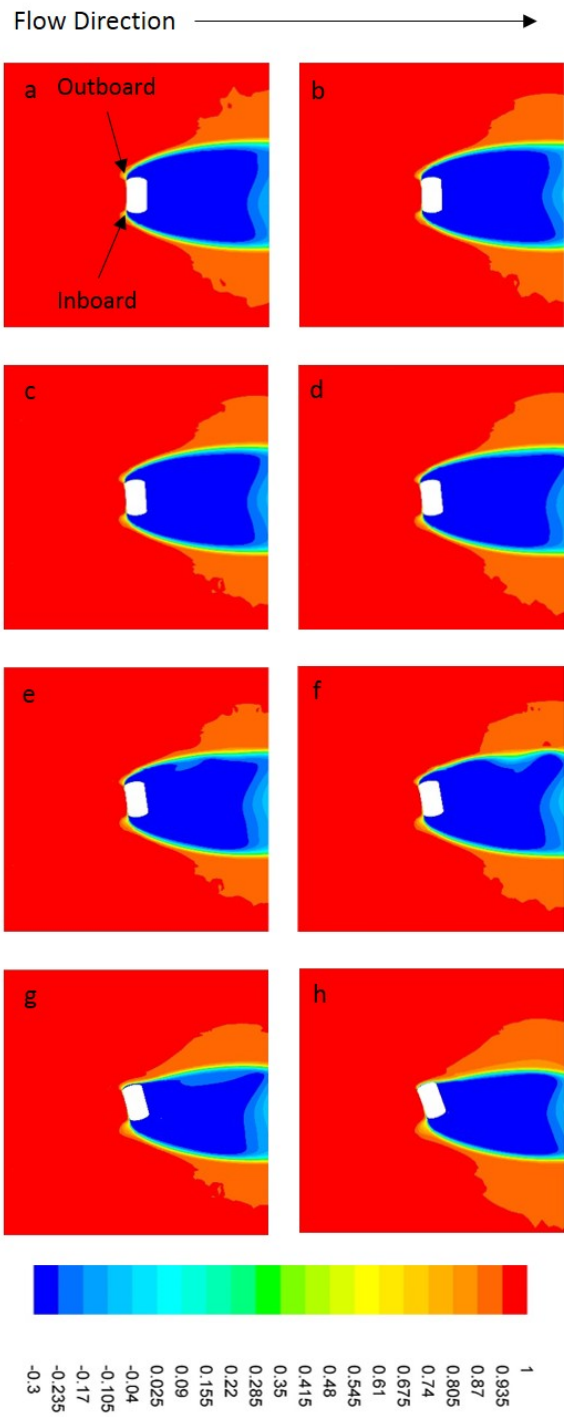

Figure 6.11: Contours of Total Pressure Coefficient at the mid plane of the contact patch – Yaw a) 0° b) 2° c) 4° d) 6° e) 8° f) 10° g) 15° h) 20°

From Figure 6.11, the reduction and increase in the flow angle can easily be observed. For smaller yaw angles this angle change is less obvious however as the

angle increases above four degrees, the change becomes more significant. Between zero and 10 degrees, the separation points at the contact patch remain the same, and the flow always separates from the leading edge. At high yaw angles, above 10 degrees, the outboard side of the contact patch became highly aligned to the flow resulting in flow which seemed to remain more attached to the contact patch and only fully separate from the trailing edge. Additionally, as the outboard side of the contact patch aligns to the flow more, the flow around the contact patch starts to skew slightly. The alignment of the side of the contact patch has contributed to large variations to the primary flow structures over the wheel and is discussed in further detail in Section 6.2.4.

6.2.3 Pressure Distribution over the Wheel Centreline

To identify possible reasons for the increase in lift and drag, the coefficient of static pressure was plotted around the centreline of the wheel. This is shown in Figure 6.12 on the following page.

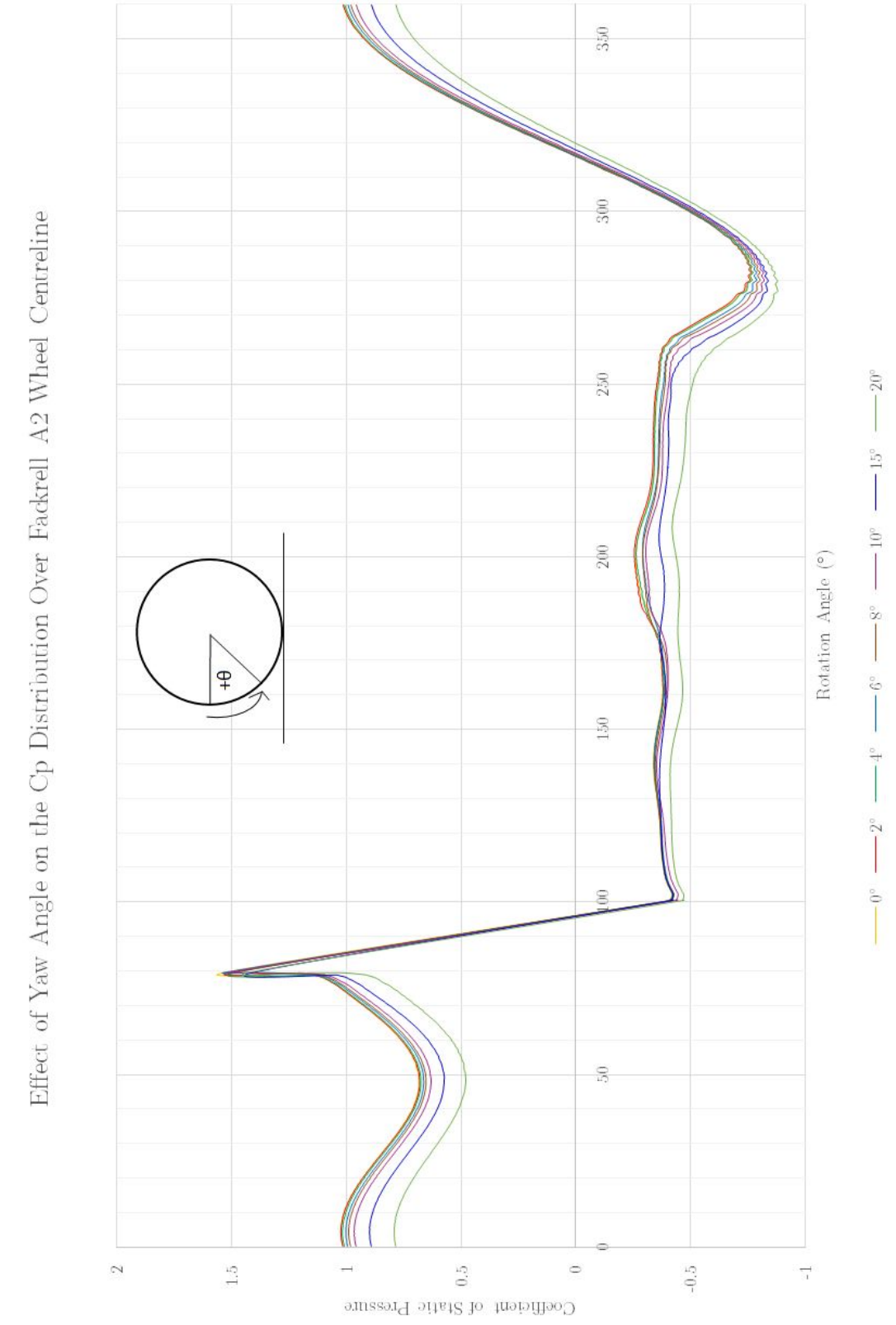

Figure 6.12: Comparison of Static Pressure Coefficient over wheel centreline – Yaw. %Error for all data ± 0.02%

From Figure 6.12, it can be seen that as the yaw angle increases areas of the curve are shifted down. This aligned with the lift data produced as an increased suction over the wheel is also observed here. The reduction in the overall pressure over the centreline is not surprising as the wheel is no longer aligned to the flow. What was surprising was that the rotation of the wheel did not have a significant effect on the positive pressure peak ahead of the contact patch and at the separation point over the rear of the wheel, even at extreme yaw angles of 15 and 20 degrees. The pressures over the centreline at these angles showed a similar trend to the remaining data. The location of the positive pressure peak was consistent regardless of the yaw angle tested, and the separation point of the flow on the top surface of the wheel also remained the same at approximately 280 degrees. This showed that the effects due to the rotation of the wheel were stronger than any disturbances due to yaw at these locations. The interaction and compression of the flow between the wheel and ground was also not affected by any yaw input.

Slight variations to the flow on the surface were observed on the rear of the wheel, from the training edge of the contact patch to the separation point on the top surface of the wheel. This variation is primarily due to the changes to the flow structures around the wheel. The interaction of the flow behind the centre of the wheel and the jetting vortices was a key reason for this.

6.2.4 Effect of Yaw on the Flow Structures around the Wheel

The contact patch had a different effect on the flow around the wheel when compared to camber. The shape of the contact patch remained constant however its alignment to the flow varied due to the applied yaw. This change had a significant effect on the primary jetting vortices. The flow around the yawed wheel was similarly visualised by using constant velocity iso-surfaces and is shown for three angles in Figure 6.13 below.

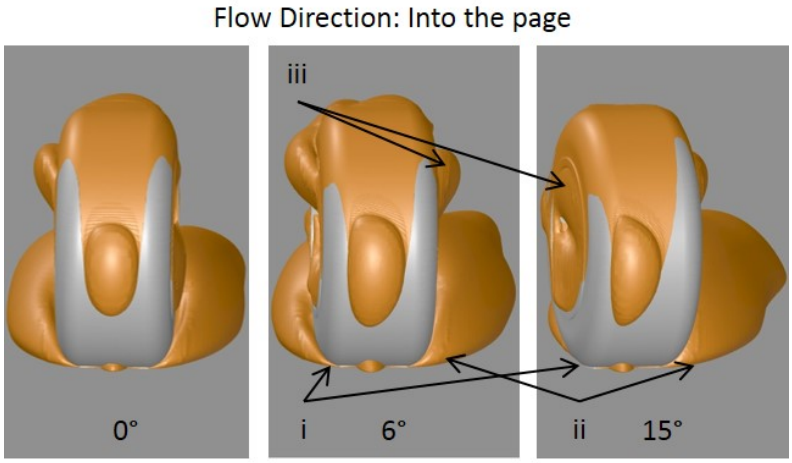

Figure 6.13: Flow structures around yawed wheel. i) Reduction in size of outboard jetting vortex ii) Increase in size of inboard jetting vortex iii) Formation of a vortex from the inboard side of rim and reduction of the outboard rim vortex.

The key areas which were identified can be seen in Figure 6.13 above. As the wheel was yawed, the amount of separation from the front of the contact patch varied, as described in Section 6.2.1. This change resulted in the two jetting

vortices becoming highly asymmetric in size. The outboard jetting vortex steadily reduced in size and the inboard jetting vortex increased (i and ii). Furthermore the outboard rim vortex was observed to slowly reduce in size as the face of wheel became more aligned with the flow. However as a result of yaw, a vortex was formed from the inboard side of the rim. This vortex was apparent from the initial yaw input of two degrees.

It was observed that as the wheel was yawed, all of the flow structures on the face of the wheel exposed to the flow started to reduce in size. In this case this was the outboard side of the wheel. The recirculation region on the top surface of the wheel was slightly skewed however the separation point on the wheel did not change as shown earlier. It was clear from the results that changes to yaw angle had a much higher impact on the flow structures in the wake of the wheel in comparison to camber. To visualise the effect of yaw on the flow in the wake, contours of total pressure coefficient were again generated at locations x/D = 0.52, x/D = 0.84 and x/D = 1.42. These are presented and discussed in the following pages.

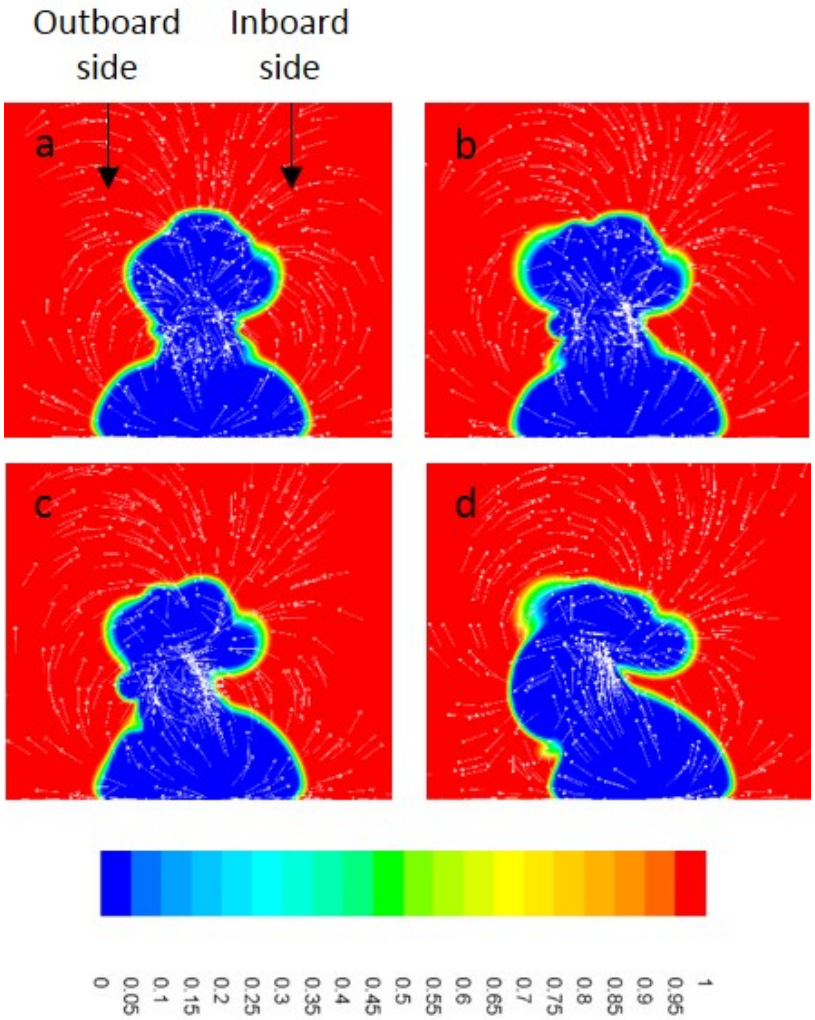

Figure 6.14: Contours of Total Pressure Coefficient located at x/D = 0.52 – Yaw. a) 2° b) 6° c) 10° d) 20°

From Figure 6.14 above, it can be seen that the yaw angle has had a drastic effect on the flow structures immediately behind the wheel. It was observed that as the angle increased the overall shape of the wake became skewed to the outboard side of the wheel. The outboard jetting vortex was seen to reduce in size and strength and was not a very dominant structure at this location. The inboard

jetting vortex was shown to influence the flow structures in the centre of the wheel and was primarily responsible for this skewness.

As the wheel rim is asymmetric, it is not unexpected that the result for two degrees yaw produced a more symmetric wake compared to zero degrees. At this location, the width of the overall wake slightly increased as the yaw increased, primarily due to the inboard jetting vortex and resulting skewed flow. The recirculation over the top surface of the wheel was shown to flatten as the yaw increased. This was expected as this region was exposed to more incoming flow as the yaw was applied.

Overall the wake displays a wide lower section with two dominating vortices tapering to smaller region of turbulence nearer to the top of the wheel. At higher yaw angles however, only the inboard jetting vortex was present at the base of the wheel resulting in an overall wake which was highly asymmetric.

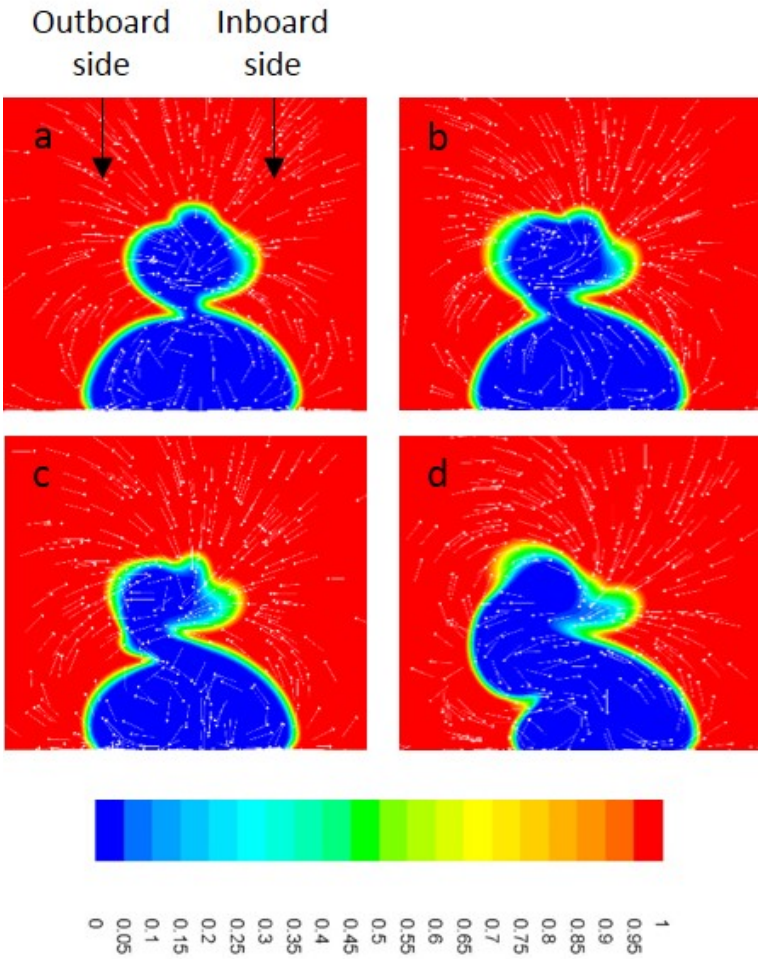

Figure 6.15: Contours of Total Pressure Coefficient located at x/D = 0.84 – Yaw. a) 2° b) 6° c) 10° d) 20°

In Figure 6.15, the flow variation immediately behind the wheel is far more pronounced when comparing the yaw angles. The central wake shape at high yaw angles showed a completely different wake profile. The inboard jetting vortex is far more dominant as the yaw angle increased compared to the previous location at $x/D = 0.52$. The effects in the wake due to the recirculation regions were observed to no longer be present to the same level. The inboard rim vortex was also observed to have greatly reduced in size and strength at higher yaw angles.

After an initial observation it was thought that the recirculating flow immediately behind the wheel from the top surface was providing some energy to the left rim vortex at higher yaw angles, and this location proves that this was the case. The left rim vortex has deteriorated and was not sustained to the same level due to the lack of the recirculating flow. By comparing the plots at two degrees and 20 degrees the deterioration of the vortex is very evident.

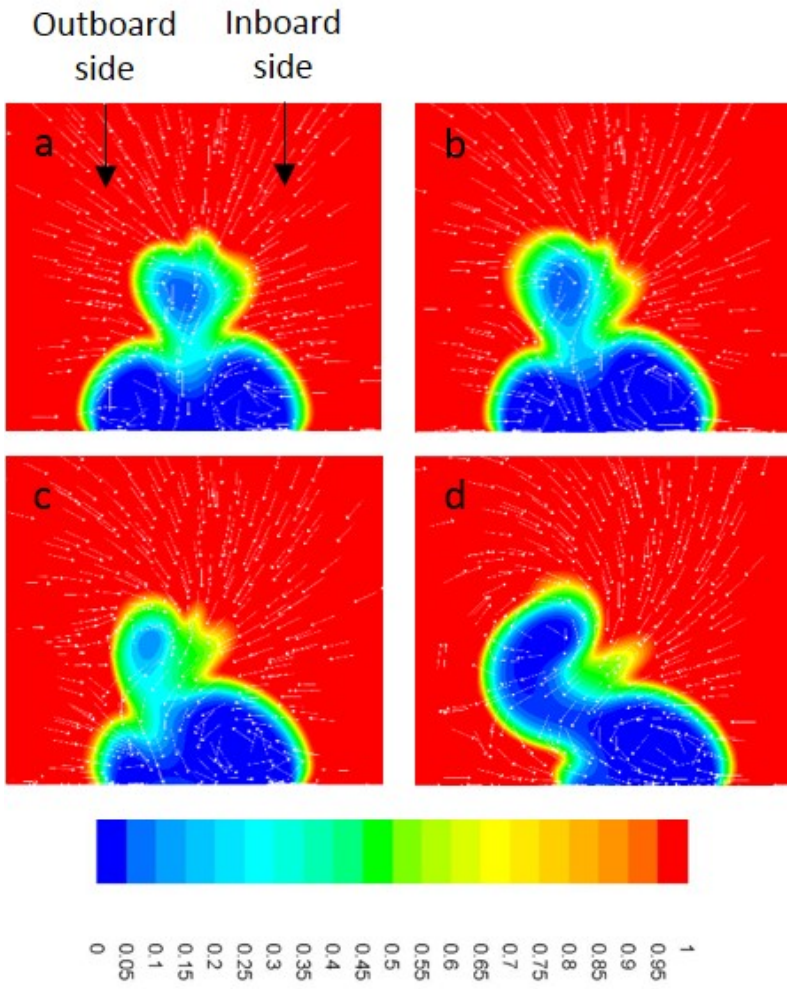

Figure 6.16: Contours of Total Pressure Coefficient located at x/D = 1.42 – Yaw. a) 2° b) 6° c) 10° d) 20°

At the location shown in Figure 6.16, the flow structures near the upper sections of the wheel have lost strength for all yaw angles aside from 20 degrees; however the jetting vortices are still strong and well defined. Again in a similar observation to the cambered wheels, the jetting vortices were the most dominant flow structures. From the contours, it can be seen that the outboard jetting vortex is deteriorating faster than the left as the yaw angle increases and at 20 degrees, the outboard jetting vortex is no longer present. The inboard vortex at this location was shown to have an increased diameter and stretch past the centre of the wheel. Additionally, at 20 degrees yaw, the flow near the upper portion of the wheel is still contains a large amount of energy and the near wake has deteriorated at faster rate. This is in contrast to all other yaw angles tested.

From the contour plots presented, it was observed that the flow features change significantly as the yaw angle is increased. The change is primarily seen in the jetting vortices and the central part of the wake. Additional plots for the other yaw angles tested are located in Appendix A.

6.3 Comparing Camber and Yaw Angle

After performing the analysis, it became apparent that camber and yaw angle each affect the overall aerodynamics of a wheel in a distinct way. However both variations to the wheel affected one key area which was the contact patch.

The primary effect camber had on the aerodynamics on the wheel was that it caused the shape of the contact patch to change shape which in turn changed the behaviour of the jetting flow ahead of the wheel. This change was due to the fact that the formation point of one of the two jetting vortices, the outboard vortex, was pushed rearward. The result of this in the wake was that the outboard jetting vortex was stronger and was maintained for a longer distance downstream of the wheel, whilst the left vortex became weaker and deteriorated faster.

Yaw on the other hand maintained the shape of the contact patch however changed its orientation to the incoming flow. This changed caused the jetting vortices to again change differ however in this case the outboard jetting vortex was shown to reduce as the yaw angle increased. Additionally the inboard vortex was shown to increase as yaw was applied. This meant that in the wake, it was the inboard jetting vortex which was maintained and stronger and the outboard vortex deteriorated. This is the complete opposite effect to what was observed with camber.

Additionally, when considering the lift on the wheel it was found that camber was far more sensitive in comparison to yaw angle. Over the range of camber angles tested the maximum variation in lift was 44.6 % compared to 17.2% over the range of yaw angles. This is significant given the small magnitude of the change. However for drag the opposite was observed. The maximum variation in drag over the entire range of angles tested was 14.4% for camber compared to 33.2% for yaw.

For a road vehicle in reality, this has several implications. Camber and yaw are set in order aid handling and performance of a vehicle. For an open wheeled vehicle, the results have shown that higher camber angles provide less lift, which is beneficial. However camber also has a large effect on cornering performance. The higher the camber angle the better the cornering agility will be however straight line performance is reduced [3, 39]. Therefore even though higher camber angles are beneficial aerodynamically they may not the optimum for use in reality. A compromise must be made. Road vehicles with wheel housings will affect the overall aerodynamics however the fundamental effects of camber will always be present.

A similar compromise must be made for yaw angle in reality. From the data presented it was shown that as the applied yaw increases the lift and drag both increase which is detrimental for vehicle performance. For toe angles (small yaw

angles which are permanent), the effects are not as noticeable, however at higher angles above six degrees, the increase in lift is substantial. Increasing the lift of a wheel would mean that the wheel is physically trying to leave the surface of the road, reducing the overall grip. This is important to consider especially for a wheel which is being steered (higher yaw angles, only for a period of time). High angles of steering input are used when approaching a corner and at this point the highest amount of grip is desirable. Based on the aerodynamics alone, it would suggest that to generate the maximum grip, the maximum input for steer on the vehicle should be based on the roads the vehicle will travel on. This would be the minimum yaw angle needed to navigate the tightest radius turn. As this is only an issue when a steering input is required it is not as detrimental aerodynamically compared to camber.

When setting up a vehicle care must be taken when setting camber angles as a slight change in magnitude will have a far greater effect on the overall lift when compared to yaw. Added care must be taken because this is a permanent change on the vehicle. When setting up a vehicle specifically for cornering, care must be taken to set the yaw angle correctly to maximise the grip. Yaw and camber should both be used in conjunction with one another to optimise the overall handling and performance of the vehicle. For standard vehicles, safety is paramount. Vehicles with aggressive handling can also be dangerous. Not

applying the optimal amounts of camber and yaw may reduce overall performance however will be safer for common everyday driving.

7 Conclusion

After conducting the computational investigation it was concluded that yaw and camber both have a significant effect on the aerodynamic performance of rotating wheels in contact with the ground, both in terms of lift and drag and on the flow structures in the wake region.

Camber affected the shape of the contact patch, the formation of the outboard vortices, and the pressure over the surface of the wheel the most significantly. It was found that the formation of the outboard vortex was delayed due to the contact patch and as a result was stronger in the wake of the wheel. Camber was shown to reduce the aerodynamic lift and drag as the camber applied increased. For safety and fuel efficiency this is beneficial. However in reality extremely high amounts of camber are detrimental to straight line performance and stability therefore a compromise must be taken between the aerodynamic benefits and the overall driveability of the vehicle.

Yaw on the other hand had an adverse effect on both the lift and drag on the wheel. It was shown that yaw increased both the lift and drag. The added drag would decrease the fuel efficiency of a vehicle. When small yaw angles are set permanently as toe, the effect on lift and drag is much smaller compared to steering at high yaw angles. Furthermore, the overall changes in aerodynamic

forces are much lower compared to camber. At higher angles not only do the forces change, the flow structures behind the wheel change significantly. Adding yaw was shown to effect reduce the size of the outboard jetting vortex and increase the size of the inboard, a stark contrast to the effects of camber. The wake shape was also highly asymmetric at higher yaw angles. It was also observed that changes to the contact patch did not affect the pressure over the surface over the wheel to the same degree as what it did to camber. For the range of yaw angles tested the maximum variation in the positive pressure peak at the contact patch was only 7% in comparison to 50% for the range of camber angles tested.

In the wake region, camber and yaw were both found to significantly affect the lower jetting vortices. However it was concluded that at higher angles, the variations in the wake due to yaw was far more detrimental to the flow in comparison to camber.

Given the fact that camber and toe angles are a permanent feature on a vehicle, it was concluded that camber is the parameter which is the most critical to set correctly. High yaw angles only occur during steer and as such the effects on the flow are only apparent for a short period of time. Furthermore in reality, variations in camber have a far more profound and noticeable effect on vehicle handling and driveability in comparison to toe.

8 Future Work

Following on from what has been presented in this thesis, many avenues may be pursued. Firstly, the next stage for computational work is to use a transient approach. There are many different transient models one can employ, however the method which is suggested for this study is the new scale-adaptive simulation (SAS) method. This method is unique because the model uses variations in mesh density to help determine where transient flow features may be present. Additionally this method maintains a RANS approach in areas where the flow is steady. A transient simulation is important as the complex flow involving vortex shedding can be captured more accurately. Computational requirements for SAS are still high however are less than DES and LES methods.

Further simulations involving a combination of camber and yaw should also be performed. Given that vehicles usually have a combination of both, it would be important to observe how the flow characteristics vary. It would be required in the future to gain a deeper understanding of the lift and drag and how the flow structures in the wake vary as a result.

An experimental investigation can be performed of a solid cambered and yawed wheel utilising measurement techniques such as particle image velocimetry (PIV) to visualise and validate the flow structures observed in the simulation results.

Experimental procedures as described by Fackrell and Mears should also be utilised to validate the pressure distribution results.

Further studies, both computational and experimental, for a rotating wheel would need to investigate the deformation of a wheel. This would primarily involve a deforming wheel shoulder. From this study the aerodynamic forces and flow structures were highly sensitive to the contact patch shape and deformation to the tyre will alter this shape further affecting the aerodynamic characteristics of the wheel. To what degree this affects the inboard and outboard vortices and surrounding flow structures is still unknown. In reality, tyres can deform due to factors including internal pressure variations and external loads and hence need to be investigated further.

References

1. Diasinos, S., et al., Computational Analysis Comparing Aerodynamic Performance of Simplified Sedan, Wagon and SUV Automobile Configurations, in FISITA 2014 World Automotive Congress2014: Maastricht, The Netherlands.

2. Katz, J., Race Car Aerodynamics: Designing for Speed. 1996.

3. Gillespie, T.D., Fundamentals of Vehicle Dynamics. 1992.

4. Fackrell, J.E., The Aerodynamics of an Isolated Wheel Rotating in Contact with the Ground, 1975, University of London.

5. Ramachandran, D. and G.C. Doig, Unsteady Flow around an Exposed Rotating Wheel, in Amercan Institute of Aeronautics and Astronautics Student Paper Conference2011.

6. Regert, T. and T. Lajos, Investigation of Flow Field Past Rotating Wheels of Cars, in The 12th International Conference on Fluid Flow Technologies2003: Budapest, Hungary.

7. Axerio, J., et al., Computational and Experimental Investigation of the Flow Structure and Vortex Dynamics in the Wake of a Formula 1 Tire. SAE International, 2009(09B-0082).

8. Axerio-Cilies, J., et al., An Aerodynamic Investigation of an Isolated Stationary Formula 1 Wheel Assembly. Journal of Fluids Engineering, 2012. 134: p. 1-17.

9. Cogotti, A., Aerodynamic Characteristics of Car Wheels. International Journal of Vehicle Design, 1983. Special Publication SP3: p. 173-196.

10. Croner, E., et al., Aerodynamci Characterization of the wake of an isolated rolling wheel. International Journal of Heat and Fluid Flow, 2013. 43: p. 233-243.

11. Geradin, F., C. Gentric, and N. Midoux, Particle Dispersion in the near-wake of a n isolated rotating wheel: Experimental and CFD Study. Journal of Aerosol Science, 2014. 76: p. 56-71.

12. Kellar, W.P., S.R.G. Pearse, and A.M. Savill, Formula 1 car wheel aerodynamics. Sports Engineering, 1998. 2: p. 203-212.

13. Knowles, R., A. Saddington, and K. Knowles, On the Near Wake of Rotating, 40% Scale Champ Car Wheels. SAE International, 2002(2002-01-3293).

14. McManus, J. and X. Zhang, A Computational Study of the Flow Around an Isolated Wheel in Contact With the Ground. Journal of Fluids Engineering, 2006. 128: p. 520-530.

15. Morelli, A., Aerodynamic Effects on the Car Wheel. ATA Review, 1969. 22(6): p. 281-288.

16. Pirozzoli, S., P. Orlandi, and M. Bernardini, The fluid dynamics of rolling whels at low Reynolds number. Journal of Fluid Mechanics, 2012. 706: p. 496-533.

17. Prasad, M.S. and S. Watkins, Vehicle wheel aerodynamic testing, using the double-symmetry technique. International Jounral of Vehicle Design, 2008. 48: p. 81-96.

18. Regert, T. and T. Lajos, The Effect of Wheels and Wheelhouses on the Aerodynamic Forces acting on Passenger Cars. 2006.

19. Saddington, A.J., R.D. Knowles, and K. Knowles, LDA Measurements in the Near-Wake of an Isolated Formula One Wheel. Experiments in Fluids, 2002.

20. Tew, G.S. and A.T. Sayers, Aerodynamics of yawed racing cycle wheels. Journal of Wind Engineering and Industrial Aerodynamics, 1999. 82: p. 209-222.

21. Axon, L., The Aerodynamic Characteristics of Automobile Wheels - CFD and Wind Tunnel Experiment, 1999, Cranfield University.

22. Bashirinia, S., et al., PANS simulations of the flow around a rotating wheel, 2011, Chalmers University of Technology.

23. Berg, M.A.v.d., Aerodynamic Interaction of an Inverted Wing with a Rotating Wheel, 2007, University of Southampton.

24. Diasinos, S., The Aerodynamic Interaction of a Rotating Wheel and a Downforce Producing Wing in Ground Effect, 2009, University of New South Wales.

25. Knowles, R.D., Monoposto Racecar Wheel Aerodynamcis: Investigation of Near Wake Structure & Support-Sting Interference, 2005, Cranfield University.

26. Mears, A.P., The Aerodynamic Characteristics of an Exposed Racing Car Wheel, 2004, University of Durham.

27. Sarmast, S., Numerical Simulation of the flow around the wheel within wheelhouse, 2010, Chalmers University of Technology.

28. Aldoss, T.K. and T.W. Abou-Arab, Experimental study of the flow around a rotating cylinder in crossflow. Experimental Thermal and Fluid Science, 1990. 3(3): p. 316-322.

29. Bearman, P.W., et al., The Effect of a Moving Floor on Wind Tunnel Simulation of Road Vehicles. SAE 1988(880245).

30. Kothalawala, T.D., A. Gatto, and L. Wrobel, Computational Investigation of the Combined Effects of Yaw, Rotation and Ground Proximity on the

Aerodynamics of an Isolated Wheel. International Journal of Mechanical, Aerospace, Industrial and Mechatronics Engineering, 2013. 7(9): p. 720-726.

31. Suspension, S., Camber Angle Schematic, http://www.carid.com/images/skyjacker/info/images/tech-terms-2.jpg, Editor.

32. Suspension, S., Yaw Angle Schematic, http://www.carid.com/images/skyjacker/info/images/tech-terms-5.jpg, Editor.

33. Tu, J., G.-H. Yeoh, and C. Liu, Computational Fluid Dynamics: A Practical Approach. 2008.

34. Versteeg, H.K. and W. Malalasekera, An Introduction to Computational Fluid Dynamics. The Finite Volume Method. 1995.

35. ANSYS, ANSYS Fluent 15.0 User Guide. 2015.

36. Menter, F.R., Two-Equation Eddy-Viscosity Turbulence Models for Engineering Applications. AIAA Journal, 1994. 32(8): p. 1598-1605.

37. Spalart, P. and S. Allmaras, A one-equation turbulence model for aerodynamics flows. 1992: p. Technical Report AIAA-92-0439. American Institute of Aeronautics and Astronautics

38. Roache, P.J., Perspective: A Method for Uniform Reporting of Grid Refinement Studies. Journal of Fluids Engineering, 1994. 116: p. 405-413.

39. Milliken, W.F. and D.L. Milliken, Race Car Vehicle Dynamics. 1994.

Appendices

Appendix A: Additional Figures – Camber and Yaw

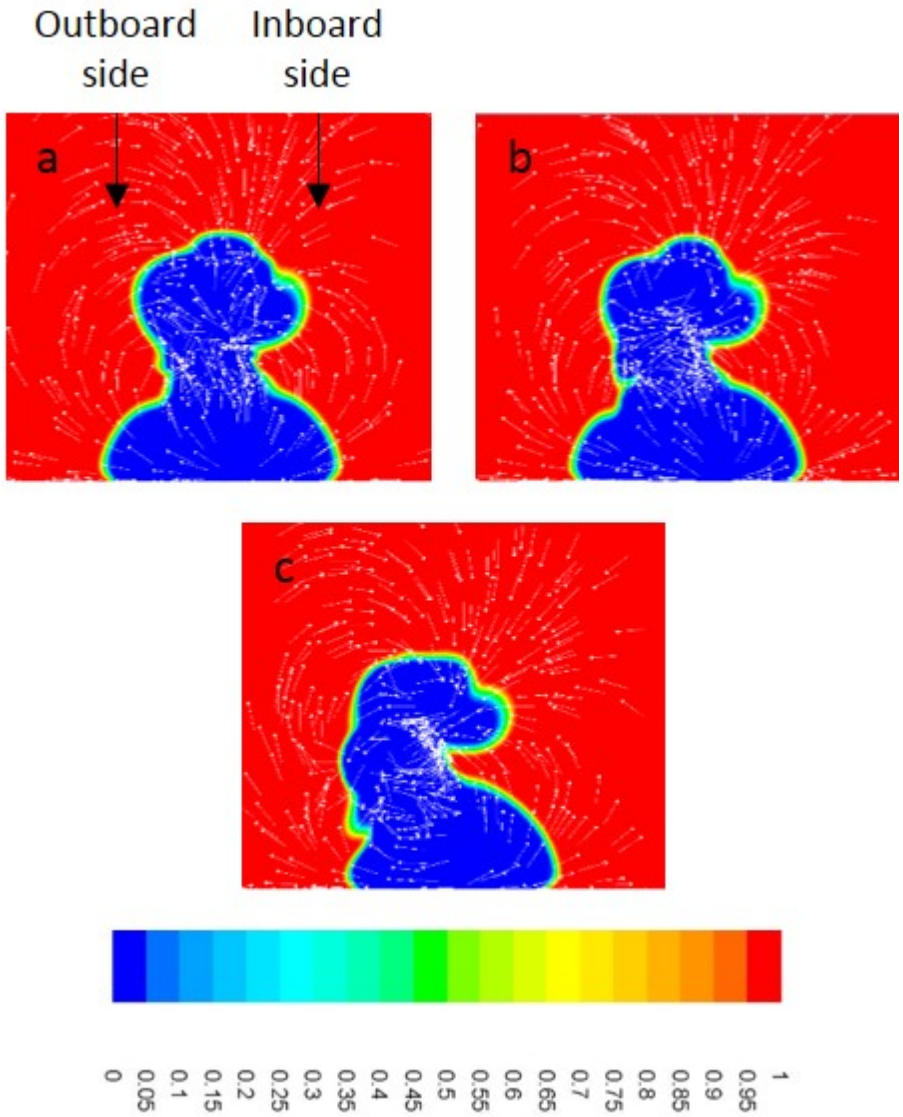

Figure A.1: Contours of Total Pressure Coefficient located at x/D = 0.52 – Yaw. a) 4° b) 8° c) 15°

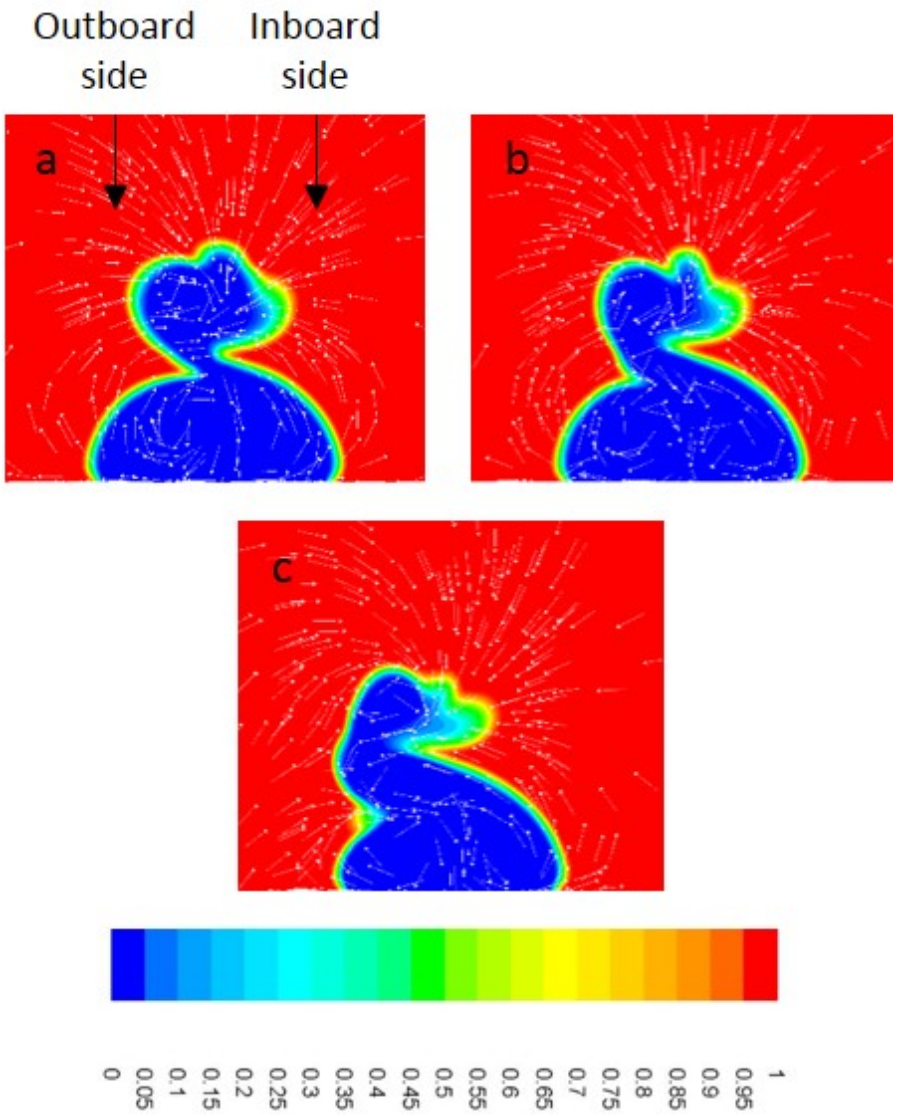

Figure A.2: Contours of Total Pressure Coefficient located at x/D = 0.84 – Yaw. a) 4° b) 8° c) 15°

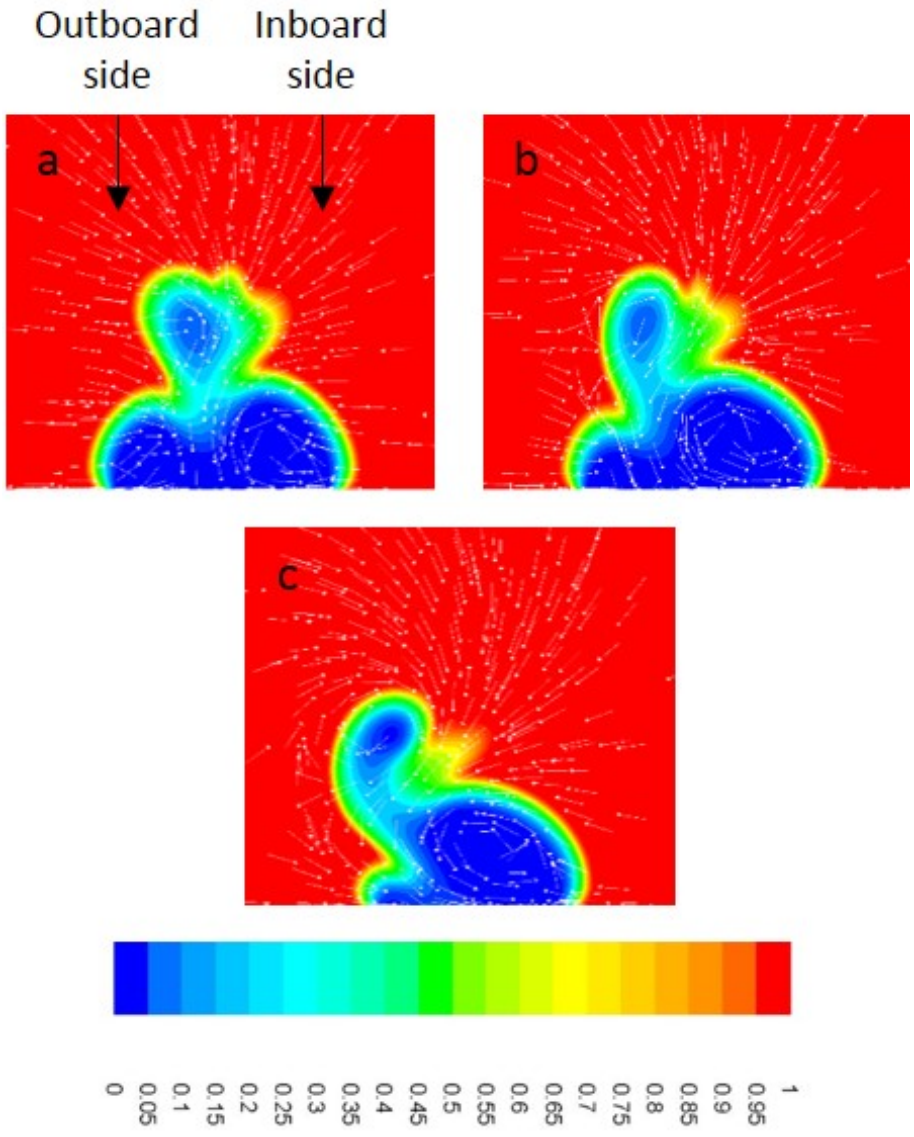

Figure A.3: Contours of Total Pressure Coefficient located at x/D = 1.42 – Yaw. a) 4° b) 8° c) 15°

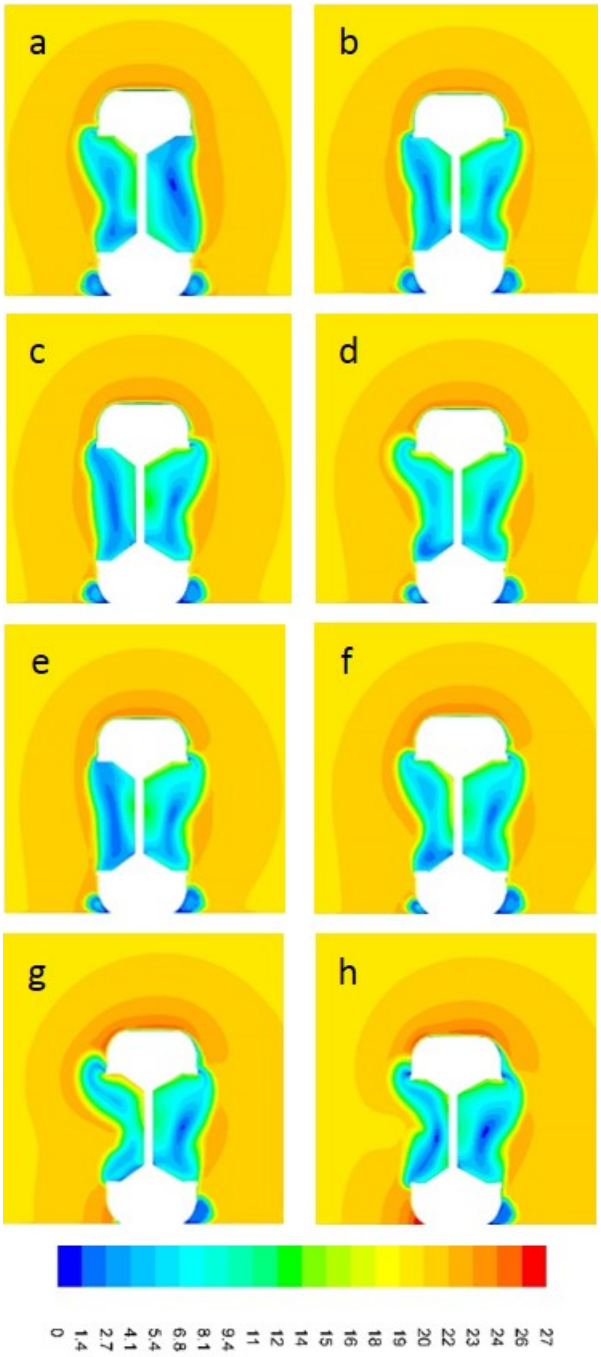

Figure A.4: Contours of Velocity Magnitude at x/D = 0 – Yaw. a) 0° b) 2° c) 4° d) 6° e) 8° f) 10° g) 15° h) 20°

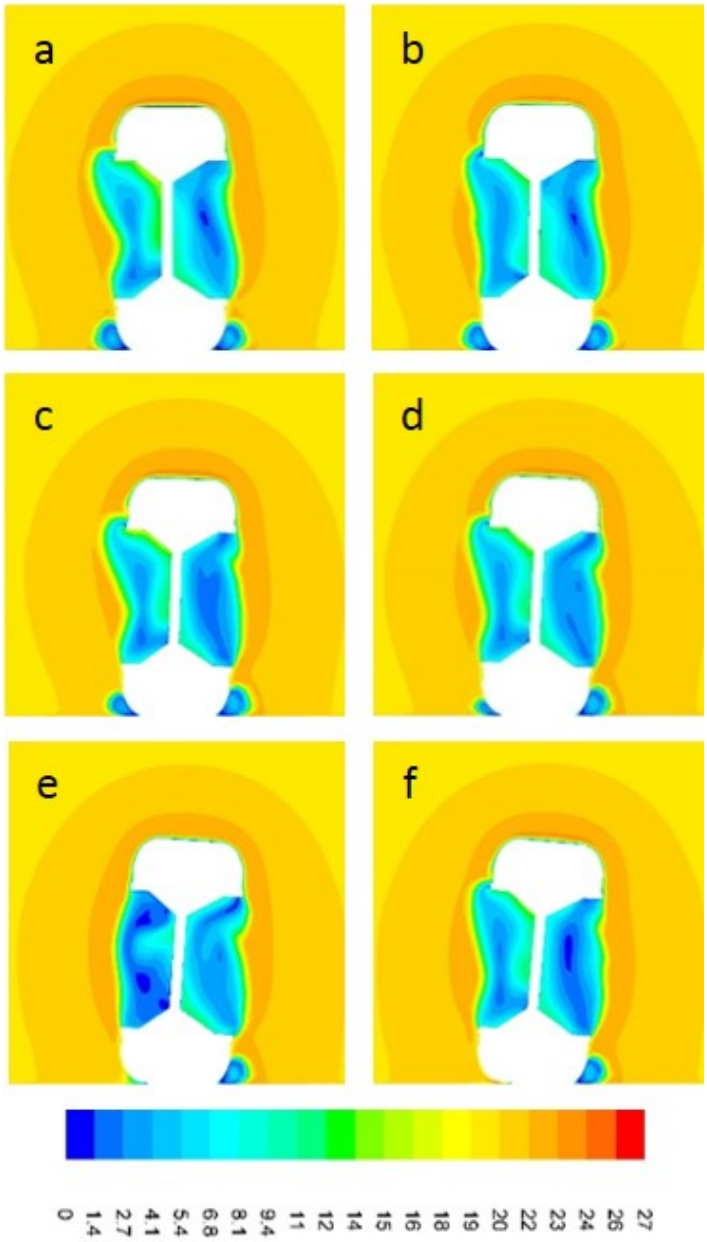

Figure A.5: f) Contours of Velocity Magnitude at x/D = 0 – Camber. a) 0° b) -1° c) -2° d) -3° e) -4° f) -5°